How to cite: *Angew. Chem. Int. Ed.* **2023**, *62*, e202316792
doi.org/10.1002/anie.202316792

Gas Separation

Molecular Sieving of Propyne/Propylene by a Scalable Nanoporous Crystal with Confined Rotational Shutters

*Jingmeng Wan, Hao-Long Zhou, Kim Hyeon-Deuk, I-Ya Chang, Yuhang Huang, Rajamani Krishna, and Jingui Duan**

Abstract: Soft porous coordination polymers (PCPs) have the remarkable ability to recognize similar molecules as a result of their structural dynamics. However, their guest-induced gate-opening behaviors often lead to issues with selectivity and separation efficiency, as co-adsorption is nearly unavoidable. Herein, we report a strategy of a confined-rotational shutter, in which the rotation of pyridyl rings within the confined nanospace of a halogen-bonded coordination framework (**NTU-88**) creates a maximum aperture of 4.4 Å, which is very close to the molecular size of propyne (C_3H_4: 4.4 Å), but smaller than that of propylene (C_3H_6: 5.4 Å). This has been evidenced by crystallographic analyses and modelling calculations. The **NTU-88o** (open phase of activated **NTU-88**) demonstrates dedicated C_3H_4 adsorption, and thereby leads to a sieving separation of C_3H_4/C_3H_6 under ambient conditions. The integrated nature of high uptake ratio, considerable capacity, scalable synthesis, and good stability make **NTU-88** a promising candidate for the feasible removal of C_3H_4 from C_3H_4/C_3H_6 mixtures. In principle, this strategy holds high potential for extension to soft families, making it a powerful tool for optimizing materials that can tackle challenging separations with no co-adsorption, while retaining the crucial aspect of high capacity.

Introduction

The chemical industry heavily relies on distillation or catalytic conversion to separate chemicals into their pure forms, particularly small gases.[1] However, this accounts for a quarter of the world's energy consumption, making it imperative to develop transitional or alternative technologies that are highly efficient, energy-saving, and low-cost. One promising technology is physio-adsorption in porous materials, which has the potential to reduce energy intensity by a factor of 10 or more. This non-thermal technology has already been successfully used in oxygen/nitrogen separation using ZMS zeolites.[2–3] However, the current and major hurdle still exists in the industry, such as the deep removal of C_3H_4 from C_3H_6, a main and large quantity raw material for the production of value-added chemicals. This is due to the fact that two molecules have very similar structure and molecular sizes (C_3H_4: 4.4×6.8 Å^2, C_3H_6: 5.4×6.8 Å^2), in addition to the low concentration of C_3H_4 (usually up to 3.6 % in companies, China) in the mixtures.[4–7]

Porous materials, specifically porous coordination polymers (PCPs), also called metal–organic frameworks, are a new type of crystalline porous materials that have shown a great potential to be used in nanopore chemistry for separation applications.[8–16] These materials possess inherent modularity and can be easily designed, making them highly suitable for energy-efficient gas recognition and accommodation. However, to establish a more effective adsorbent, the sieving properties of PCPs should be considered firstly, exemplified by the rigid frameworks of KAUST-7 (C_3H_6/C_3H_8 splitter) and the UTSA-280 (C_2H_4/C_2H_6 sieve).[17–18] Notably, there are significant challenges in designing and constructing rigid pores with perfect size/shape for sieving C_3H_4/C_3H_6 mixtures, especially considering the more or less inherent flexibility of coordinated porous frameworks.

Comparably, soft PCPs, an unique class of porous materials that exhibit stimulus-responsive phase transformations, have been considered as one of the most exciting discoveries in recent.[19–27] These materials can be designed to be sensitive to different guests, but, co-adsorption is a common challenge once the pore was opened. Therefore, we here believe that the strategy of confined-rotational shutters is expected to break through this limitation, as the confined space within the micro-porous framework (2.5–4.0 Å) determines the trajectory of the rotating unit, allowing structural changes under external stimuli to meet the requirements for molecular sieving of these two similar molecules. This approach will effectively prevents co-adsorption, which usually occurs in other soft frameworks due to random or significant changes. Although soft PCPs, including layer sliding, framework distortion, flexible nodes or dynamic gating, have been extensively reported,[28–32] the challenge

[*] J. Wan, Y. Huang, Prof. Dr. J. Duan
State Key Laboratory of Materials-Oriented Chemical Engineering, College of Chemical Engineering, Nanjing Tech University
211816 Nanjing (China)
E-mail: duanjingui@njtech.edu.cn
Prof. Dr. H.-L. Zhou
Department of Chemistry, Shantou University
515063 Shantou (China)
Prof. Dr. K. Hyeon-Deuk, Dr. I-Y. Chang
Department of Chemistry, Kyoto University
606-8502 Kyoto (Japan)
Prof. Dr. R. Krishna
Van 't Hoff Institute for Molecular Sciences, University of Amsterdam
Science Park 904, 1098 XH Amsterdam (The Netherlands)

remains in achieving an open phase that can effectively prevent co-adsorption of gas pairs with extremely similar properties, while still maintaining a high adsorption capacity for the recognized molecule.[27,33]

During our exploration in soft materials,[18,33–34] we recently developed a confined strategy involving the use of water nanotubes within a robust framework. Thanks to the protection provided by this framework, the confined water nanotubes exhibited exclusive adsorption of C_3H_6, but not C_3H_8. However, the lower porosity of the water nanotubes has motivated us to develop a new system. In this work, we report a strategy of confined-rotational shutters (Scheme 1), where the rotation of pyridyl rings from the ligand (**L**: 4,4′-dipyridylnitride) in the nanospace of a halogen-bonded framework boosts the sieving separation of C_3H_4/C_3H_6 mixtures. Furthermore, the accurate identification of gas-induced transition structures provides valuable insights into the separation mechanism at the molecular-level.

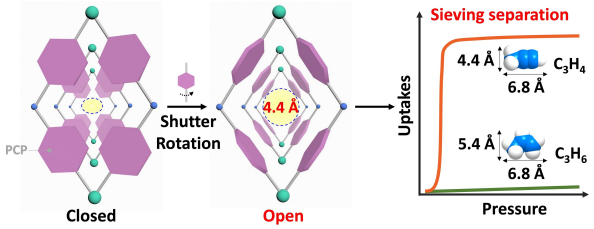

Scheme 1. Illustration of the confined-rotational shutters strategy in micro-porous crystals for sieving of C_3H_4/C_3H_6 mixtures by eliminating co-adsorption.

Results and Discussion

Green rhombus-shaped crystals (**NTU-88**) were obtained through a solvothermal reaction of 4, 4′-dipyridylnitride (**L**) and $NiCl_2 \cdot 6H_2O$ in *N,N′*-dimethylformamide/ethanol/H_2O. Single-crystal X-ray diffraction (SCXRD) structural analysis revealed that it crystallizes in the orthorhombic system with *P*bcn space group (Table S1).[35] The asymmetric unit consists of half a Ni^{2+} cation, one Cl^- anion, and one ligand, giving the formula $[Ni(\mathbf{L})_2Cl_2]\cdot x$Solvent for **NTU-88**. Each ligand is connected to two Ni ions, while, four N atoms from four ligands and two charge balanced Cl^- anions complete the coordination geometry of the mononuclear nickel node (Figure S2). Therefore, a typical **sql** layer with a rhombus pore of 5.3×8.8 $Å^2$ was established. In addition, with a side length of 11.232 Å, the angle of ∠Ni–Ni–Ni in the rhombus pore is 108.87° (Figure 1a). The adjacent AB layers are stacked together through the formation of relatively strong hydrogen bonds ($d_{Cl\cdots H-N}$: 2.363 Å), creating a supramolecular structure. Additionally, the two coordinated Cl atoms form hydrogen bonds with the H atoms from the four pyridine rings (Figure S3–S4 and Table S2), resulting in a restricted configuration of the pyridine rings (dihedral angle: 55.41°) in the V-shaped ligand. Additionally, the substantial rhombus pore present in the single layer has been tailored into a one-dimensional (1D) zigzag channel (3.2×5.6 $Å^2$) within the packed frameworks (Figure 1b–1c).

The structures and phase purities of the as-synthesized **NTU-88** were confirmed by PXRD analysis (Figure S7). After exchanging the guest with dry methanol, the fully activated **NTU-88** was obtained by degassing under high vacuum at 373 K according to the thermogravimetric (TG) results (Figure S8). However, the diffraction pattern of the desolated crystals (**NTU-88c**) was different, indicating a structural transformation. Based on this pattern, the structure of **NTU-88c** was established by Pawley refinement

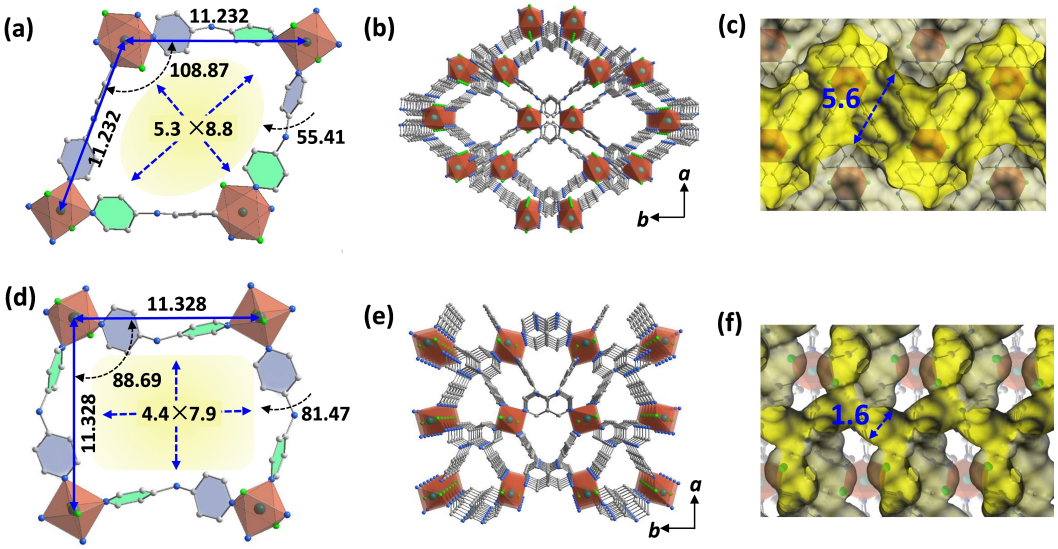

Figure 1. Structural comparison: Single-layer (a), multi-layers (b) and accessible inner pore (c) of **NTU-88**; Single-layer (d), multi-layers (e) and accessible inner pore (f) of **NTU-88c**. Units for distances and angles are Å and °, respectively.

(Figure S10 and Table S3). The crystal system changed to monoclinic with a $P2_1/c$ space group. Although the coordination connections of the metal node and organic linker remained the same as before, the configuration of the pore in the single layer underwent a significant change. The initial rhombus pore changed into a nearly rectangular one (4.4×7.9 Å^2) with an angle of ∠Ni–Ni–Ni of 88.69°. In addition, a rotation occurred on the pyridine ring, giving a dihedral angle of 81.47°. Meanwhile, the initial accessible pore in **NTU-88** was tailored into a state with a very tiny pore (1.6 Å) (Figure 1d–1f).

Considering the framework change after activation, it was expected that the framework of **NTU-88c** would undergo structural changes during gas adsorption. The permanent porosity of **NTU-88c** was analysed by CO_2 (195 K) and N_2 (77 K) adsorption isotherms (Figure 2a). Negligible N_2, but significant CO_2 uptake, were observed. The adsorption of CO_2 can be divided into two stages: a gradual increase before reaching $P/P_0 = 0.015$ followed by a sudden increase. Based on the CO_2 adsorption isotherm, the Brunauer–Emmett–Teller (BET) surface area was calculated to be $\approx 420\ m^2 \cdot g^{-1}$. Giving this observation, single-component adsorption isotherm of C_3H_4 was collected at 298 K (Figure 2b). Similarly, the isotherm showed a two-step adsorption process, with a rapid uptake occurring at about 15.6 kPa. Further, in situ PXRD analysis during the adsorption-desorption process revealed a notable phenomenon. The peaks corresponding to the [−1 1 1] and [0 3 1] planes exhibit a gradually shifted to a lower angle as the pressure initially increased, indicating a slight expansion of the *AB*-layers and the angle of the V-shaped ligand. Interestingly, the peaks associated with the [1 0 0] and [−1 1 1] crystal planes merged into a single peak at about $2\theta = 11.1°$, showing the formation of a new phase (Figure 2c and S11–S12). This significant change is consistent with the sudden C_3H_4 uptake. In addition, the PXRD patterns did not show any observable changes until the pressure decreased to 10 kPa. Interestingly, when the pressure decreased to 5 kPa, the merged peak splits into two, with positions consistent with that of **NTU-88c**, indicating the reversibility of structural changes.[29] On the contrary, the PXRD patterns under a C_3H_6 atmosphere did not show any changes throughout the pressure range (Figure 2d and S13).

To explore the reason for the significant differences observed, structural models have been established based on the in situ PXRD data at three representative pressure (8 kPa: **NTU-88α**, 14 kPa: **NTU-88β** and 100 kPa: **NTU-88o**) for C_3H_4 (Figure S10, S14–S15). A comparison of the structures of **NTU-88c**, **NTU-88α** and **NTU-88β** revealed only minor structural change. However, as the pressure increased, there was a gradual increase in the angle of ∠Ni–Ni–Ni in the rhombus pore, from 88.69° up to 89.22°, as well as an increase in the distance between metal nodes (from 11.328 Å to 11.366 Å). Additionally, the pore size of the packed framework also exhibited a slightly increase, from 1.60 to 1.67 Å, as the pyridine rings of the pore wall in these three states were all parallel to the *c*-axis (Figure 3a–3f). Sharply in contrast, a rotation of the pyridine rings in **L** was observed in **NTU-88o**, and the corresponding dihedral angle decreased from 81.38–81.54° in **NTU-88α** and **NTU-88β** to 55.62°. In addition, further sliding and expansion of the adjacent layers yield an enlarged pore size of the

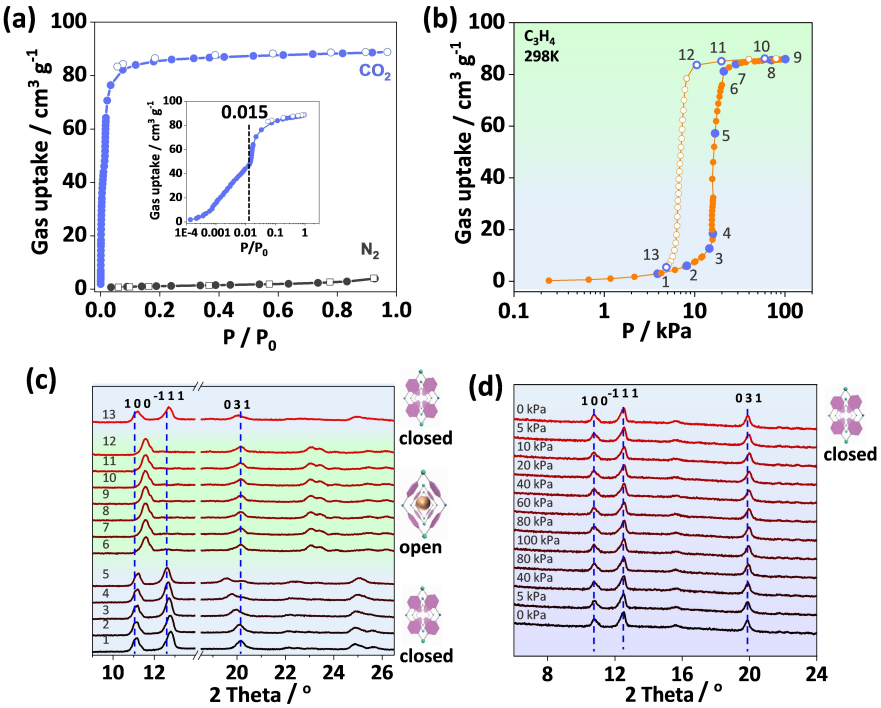

Figure 2. CO_2 (195 K) and N_2 (77 K) adsorption isotherms of **NTU-88** (a); C_3H_4 adsorption isotherm ((b), 298 K) of **NTU-88** and corresponding in-situ XRD during adsorption (c); In-situ XRD of **NTU-88** under C_3H_6 (d). All PXRD patterns were collected at 298 K.

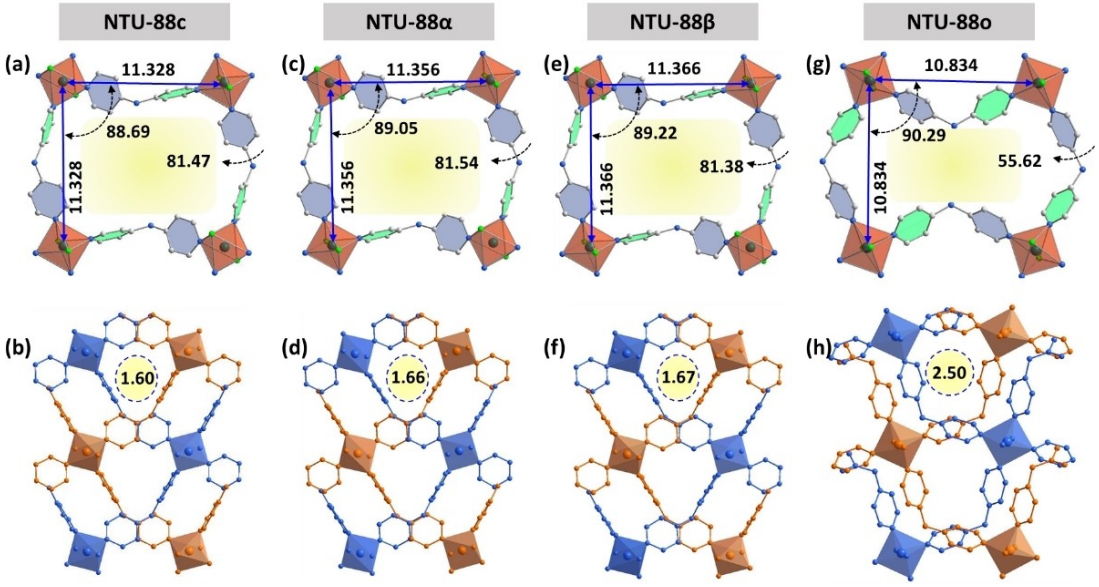

Figure 3. Structural views of **NTU-88** in different states: closed phase of **NTU-88c** (a, b); phase **α** under C_3H_4 at 8 kPa (c, d); phase **β** under C_3H_4 at 14 kPa (e, f); open phase of **NTU-88o** under C_3H_4 at 100 kPa (g, h). The corresponding temperature for all phases is 298 K. Units for distances and angles are Å and °, respectively.

packed layers, of about 2.5 Å (Figure 3g–3 h, S16–S17). Taking the molecular size of C_3H_4 in mind, this relatively small aperture would not allow for a large amount of C_3H_4 adsorption.

To elucidate this phenomenon, density functional theory computations were performed. First, we calculated the electronic density surface to estimate the van der Waals radii of the static pores in the gas channels of **NTU-88c** and **NTU-88o**. The diameters of the narrowest pores of the gas channels, 1.6 Å in **NTU-88c** and 2.5 Å in **NTU-88o**, are too short for both C_3H_4 and C_3H_6 to pass through (Figure 4a–4d). Even the diameters of the broadest pores, 2.4 Å in **NTU-88c** and 3.2 Å in **NTU-88o**, are still shorter than the shortest diameter of C_3H_4 (4.4 Å) and C_3H_6 (5.4 Å) (Figure S18–S19). Therefore, the electronic density surfaces based on the static structures cannot rationalize the present gas sieving. By introducing the rotation of the pyridine rings, we estimated the largest dynamic pore size, which occurs when the faces of the pyridine rings are almost parallel to the *c*-axis, minimizing steric hindrance for gas flow (Figure S20). The diameter of the broadest dynamic pore in **NTU-88c** is still only 3.4 Å, indicating that neither C_3H_4 nor C_3H_6 can pass through **NTU-88c** even with the rotation of pyridine rings (Figure 4e). In contrast, the diameter of the largest dynamic pore in **NTU-88o** is 4.4 Å, which is quite close to the diameter of C_3H_4 but still shorter than the diameter of C_3H_6 (Figure 4f). This means that while C_3H_6 cannot pass through this path in **NTU-88o**, but C_3H_4 can. Therefore, the pyridyl rings in the defined channel in **NTU-88** can be regarded as a confined-rotational shutter, playing a crucial role in the exclusive C_3H_4 adsorption.

The plausible confined-rotational shutter inspired us to explore the adsorption behaviors of C_3H_4 and C_3H_6 on **NTU-88**. The adsorption isotherms of C_3H_4 and C_3H_6 were collected at ambient temperatures and the results showed that the C_3H_4 uptake is as high as 86.0 $cm^3 \cdot g^{-1}$ at 1 bar, 298 K. Interestingly, the maximum uptakes are similar in the temperate range of 273 to 328 K, with only an advanced or delayed pressure for the shutter to open. As expected, C_3H_6 was nearly not adsorbed by **NTU-88** at these temperatures, as its molecular size is larger than the aperture size of **NTU-88o** (4.4 Å: shutter opening) (Figure 5a, S21–S23). Therefore, the results here suggest that the confined-rotational shutter strategy shows great promise in suppressing the co-adsorption of gas pairs with extremely similar properties, a common issue in non-restricted soft frameworks.

The significant differences in adsorption isotherms between C_3H_4 and C_3H_6 make **NTU-88o** stand out among all reported PCPs, with a maximum value of 52.7 (100/100 kPa, 298 K), and it remains almost as a constant (57.1) until the partial pressure of C_3H_4 drops below 20 kPa. In addition, the temperature-dependent shutter opening allows for a high uptake ratio of C_3H_4/C_3H_6, reaching (34.5, 4/96 kPa) at 273 K, which is also the highest among all porous materials. However, the uptake ratio is low at 1 kPa/99 kPa, 298 K, as the rotation of pyridyl rings not occurs at this condition (Figure 5b, S24–S27 and table S4).

To better understand this observation, a structural analysis of C_3H_4-loaded **NTU-88o** was performed (Figure S28–S29). The C_3H_4 molecules were found to be accommodated in the nano-channels of **NTU-88o**. Different with the open shutter in dynamic calculation, the pyridine rings rotate back and form a closed accommodation for C_3H_4 storage. In addition, the C_3H_4 molecules form a compacted and ordered 1D molecular array in the nano-channel. More interestingly, each C_3H_4 molecule forms six hydrogen bonds with adjacent carbons from the pyridine rings, with distance ranging from 2.731–2.921 Å (Figure 5c–

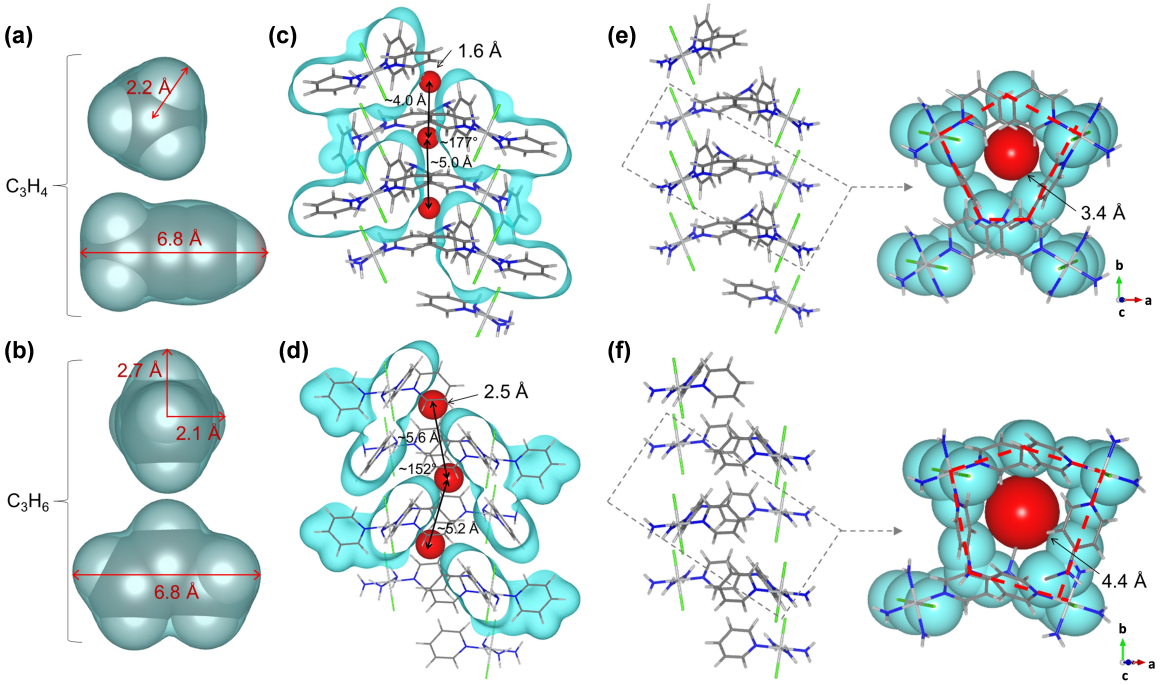

Figure 4. Effective size of C_3H_4 (a) and C_3H_6 (b); static channels existing in **NTU-88c** (c) and **NTU-88o** (d); dynamic channels appearing in **NTU-88c** (e) and **NTU-88o** (f) when the faces of the pyridine rings become almost parallel to the *c*-axis. The red dashed lines in (e, f) describe the pore boundary composed of the Ni atoms as well as the C and N atoms on the rotational axials of the pyridine rings. The light blue regions express the van der Waals radii that determine the effective pore size. The red balls indicate the effective pore size.

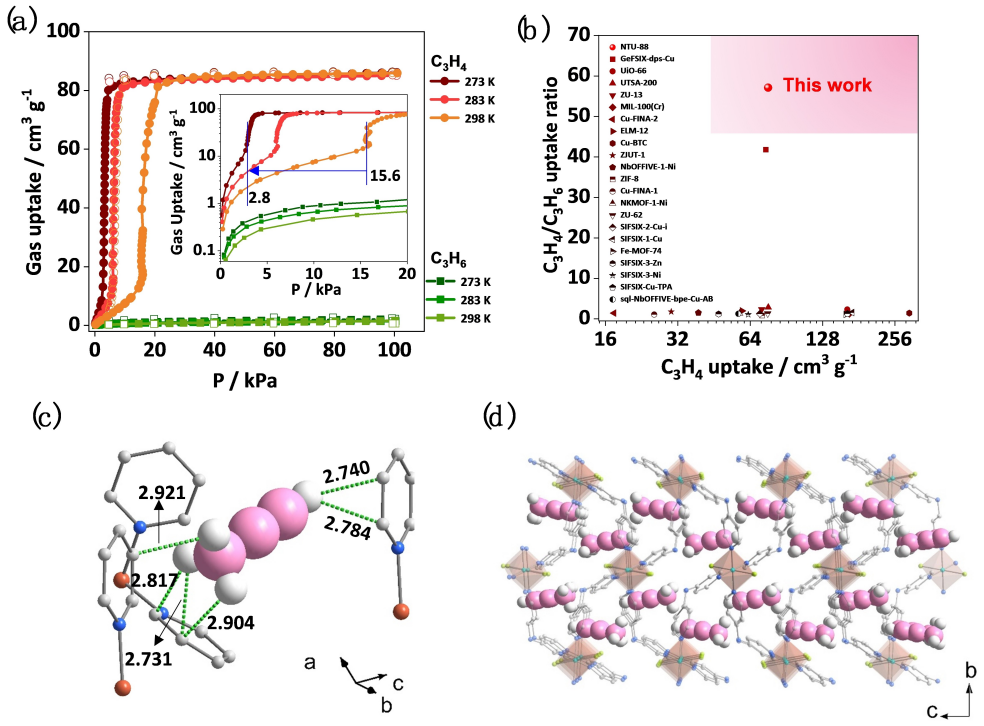

Figure 5. C_3H_4 and C_3H_6 adsorption isotherms of **NTU-88** (a), with the inset showing the re-arranged isotherms at 0–20 kPa; comparison of the C_3H_4/C_3H_6 uptake ratio (20/80 kPa, 298 K) between **NTU-88** and other materials (Table S4) (b); views of the hydrogen bonds of C_3H_4 in **NTU-88o** (c) and C_3H_4 array in **NTU-88o** (d). The gas-loaded crystal analysis was performed at 298 K.

5d). Particularly, the distances of two $\mathbf{C}_{\text{pyridine}}\cdots\mathbf{H}\text{–}\mathbf{C}_{\text{alkyne}}$ bonds are slightly shorter than the sum of the van der Waals radii of the H (1.11 Å) and C (1.72 Å) atoms, reflecting strong host-C_3H_4 interactions, as confirmed further by the relative higher isosteric heat (29.4–44.0 kJ/mol) of adsorption for C_3H_4 (Figure S30–S33, Table S5). Therefore, it is clear that the C_3H_4 molecule, due to its smaller size and stronger interactions with the framework, can open the closed shutters and achieve remarkable adsorption, whereas, the C_3H_6 molecule, being larger in molecular size and having weaker host–guest interactions, is unable to enter the framework throughout the pressure from 0—100–0 kPa at temperature range of 273 to 328 K.

Encouraged by the functions of the confined-rotational shutter, separation ability of **NTU-88** for C_3H_4/C_3H_6 mixtures was evaluated by breakthrough experiments (Figure S34–S42). After introducing an equlimolar feed gas (v/v, 1/1, 2 mL·min^{-1}) into the sample bed, polymer-grade C_3H_6 (99.95 %) elutes out at 11 min and continuing until 49 min at 298 K (Figure 6a). By changing the feed gas to C_3H_4/He (v/v, 1/1, 2 mL·min^{-1}), the curve for C_3H_4 is almost identical to that of the feed gas of C_3H_4/C_3H_6, providing conclusive evidence of complete inhibition of co-adsorption between C_3H_4 and C_3H_6 in **NTU-88**. In addition, the presence of C_3H_8 had a negligible effect on the inhibition of co-adsorption (Figure S43–S44). To further explore the function of the shutter at low C_3H_4 partial pressure, C_3H_4/C_3H_6 mixtures with a changed ratio (v/v, 1/99) were then tested. The breakthrough point for C_3H_6 was similar to that of the feed gas with an equimolar mixture, while the retention time of C_3H_4 extends to 104 min. However, it has been observed that as the velocity of the feed gas increased, the breakthrough points for C_3H_6 occurred earlier, along with the early elution of C_3H_4, (Figure 6b). Interestingly, the capacity for captured C_3H_4 remained almost unchanged at different velocities (10 mL·min^{-1}: 1.50 mL; 5 mL·min^{-1}: 1.53 mL; 2 mL·min^{-1}: 1.60 mL; 1 mL·min^{-1}: 1.63 mL), indicating that the gas speed had a negligible influence on the shutter rotation. Furthermore, during the time interval between C_3H_4 and C_3H_6 breakthrough, the high-purity C_3H_6 productivity (>99.95 %) of **NTU-88** from the outlet effluent was estimated to be 2.42 mmol·g^{-1} (298 K), which was sharply improved by reducing the temperature (4.10 mmol·g^{-1}, 271 K, Figure S42). To validate the exclusive C_3H_4 capture, desorption of the breakthrough experiment was collected. The saturated sample bed was swept with flowing N_2 (5 mL·min^{-1}) until no C_3H_6 is detected. The samples bed was then rapidly heated to 373 K, resulting in the elution of highly pure of C_3H_4 (99.95 %) (Figure S37), showing the positive effect of the confined-rotational shutter in C_3H_4 storage. Thanks to the good robustness of this framework, cycling breakthrough experiments demonstrated no capacity loss (Figure 6c and S38).

As an important factor, large-scale preparation of porous adsorbents has received widespread attention. The preparation of **NTU-88** on a large-scale (≈60 g) has been achieved by a string the corresponding ligand and metal ion in solution for only 1 min with the addition of ammonia at room temperature (Figure 6d). Obviously, this facile preparation can be scaled up to kilogram-level production. The phase purity of the microcrystals prepared on a large-scale was confirmed by PXRD analysis, and their stability was demonstrated by maintaining the same diffraction pattern even after being exposed to air for a duration of 11 months

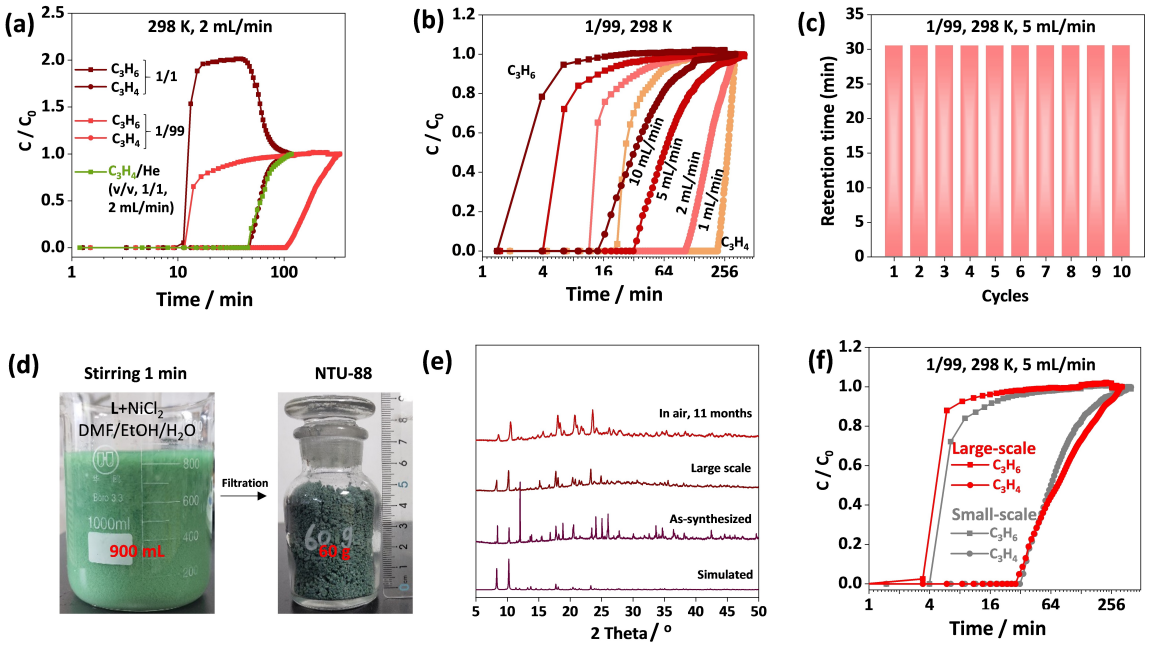

Figure 6. Experimental breakthrough curves of **NTU-88** for C_3H_4/C_3H_6 and C_3H_4/He (a); breakthrough curves of **NTU-88** for C_3H_4/C_3H_6 at different velocities (b); cycling breakthrough curves of **NTU-88** for C_3H_4/C_3H_6 (c); photos of the large-scale synthesis (d); PXRD of **NTU-88** (e); breakthrough curves of large-scale and small-scale synthesized **NTU-88** (f). All experiments were conducted at a pressure of 1 bar.

(Figure 6e). Meanwhile, the porosity and the function of the confined-rotational shutters were validated through static C_3H_4 and C_3H_6 adsorption isotherms, as well as the dynamic breakthrough experiments (Figure 6f and S45).

Conclusion

On the demand of highly pure C_3H_6, we here report a soft crystal with a confined-rotational shutter that can effectively sieve C_3H_4/C_3H_6 mixtures. The rotated pyridine ring in the nanospace creates a maximum aperture of 4.4 Å that allows exclusive C_3H_4 adsorption, but not C_3H_6. With a record high uptake ratio, good capacity, scalable synthesis and good stability, **NTU-88** holds great potential for feasible C_3H_4/C_3H_6 separation. Furthermore, the identification of transition structures during gas-induced phase change greatly enhances our comprehension of the pore-gating effect in flexible structure-types. Moving forward, this strategy has high potential to be extended to future analogues, thereby creating an important opportunity to develop optimized materials for challenging separations with high capacity and no co-adsorption.

Supporting Information

The single crystal diffraction data for NTU-88 series were deposited in the Cambridge Crystallographic Data Centre (CCDC) and the deposition numbers are 2266630–2266634.

Acknowledgements

We thank the financial support of the National Natural Science Foundation of China (22171135), the Innovative Research Team Program by the Ministry of Education of China (IRT-17R54) and the National Natural Science Foundation of Jiangsu Provience (BK20231269). K. H. D. thanks Kusunoki 125, PRESTO, Japan Science and Technology Agency Grant No. 22713147, Grant-in-Aids for Scientific Research from Japan Society for the Promotion of Science (KAKENHI) Grant Nos. 20K05419 and 18H05407, and Toyota Mobility Foundation.

Conflict of Interest

The authors declare no conflict of interest.

Data Availability Statement

The data that support the findings of this study are available in the supplementary material of this article.

Keywords: Confined-Rotational Shutters · Gas Separation · Molecular Sieving · Nanoporous Crystals

[1] D. S. Sholl, R. P. Lively, *Nature* **2016**, *532*, 435.
[2] J. C. Santos, A. F. Portugal, F. D. Magalhaes, A. Mendes, *Ind. Eng. Chem. Res.* **2006**, *45*, 1085.
[3] S. Eteve, L. Hay, T. Rottner, US patent, US5223004 A, **1993**.
[4] B. Zhu, L. Li, H. Lin, W. Han, D. Tan, F. Zhang, *Chem. Ind. Eng. Prog.* **2012**, *316*, 1379.
[5] H. Gao, B. Gao, J. Zhang, Z. Yu, *Qilu Petrochem. Technol.* **1999**, *27*, 247.
[6] H. Ma, X. Zhang, X. Zhao, *Pet. Process. Petrochem.* **2004**, *35*, 23.
[7] M. F. Friedrich, M. Lucas, P. Claus, *Catal. Commun.* **2017**, *88*, 73.
[8] H. Furukawa, K. E. Cordova, M. O'Keeffe, O. M. Yaghi, *Science* **2013**, *341*, 1230444.
[9] Y. B. Zhang, H. L. Zhou, R. B. Lin, C. Zhang, J. B. Lin, J. P. Zhang, X. M. Chen, *Nat. Commun.* **2012**, *3*, 1654.
[10] S. H. Yang, A. J. Ramirez-Cuesta, R. Newby, V. Garcia-Sakai, P. Manuel, S. K. Callear, S. I. Campbell, C. C. Tang, M. Schroder, *Nat. Chem.* **2015**, *7*, 121.
[11] J. W. Yoon, H. Chang, S. J. Lee, Y. K. Hwang, D. Y. Hong, S. K. Lee, J. S. Lee, S. Jang, T. U. Yoon, K. Kwac, Y. Jung, R. S. Pillai, F. Faucher, A. Vimont, M. Daturi, G. Ferey, C. Serre, G. Maurin, Y. S. Bae, J. S. Chang, *Nat. Mater.* **2017**, *16*, 526.
[12] C. Gu, N. Hosono, J. J. Zheng, Y. Sato, S. Kusaka, S. Sakaki, S. Kitagawa, *Science* **2019**, *363*, 387.
[13] H. Z. Wang, Z. L. Shi, J. J. Yang, T. Sun, B. Rungtaweevoranit, H. Lyu, Y. B. Zhang, O. M. Yaghi, *Angew. Chem. Int. Ed.* **2021**, *60*, 3417.
[14] P. Q. Liao, N. Y. Huang, W. X. Zhang, J. P. Zhang, X. M. Chen, *Science* **2017**, *356*, 1193.
[15] L. B. Li, R. B. Lin, R. Krishna, H. Li, S. C. Xiang, H. Wu, J. P. Li, W. Zhou, B. L. Chen, *Science* **2018**, *362*, 443.
[16] Z. Shi, Y. Tao, J. Wu, C. Zhang, H. He, L. Long, Y. Lee, T. Li, Y.-B. Zhang, *J. Am. Chem. Soc.* **2020**, *142*, 2750.
[17] A. Cadiau, K. Adil, P. M. Bhatt, Y. Belmabkhout, M. Eddaoudi, *Science* **2016**, *353*, 137.
[18] R. B. Lin, L. B. Li, H. L. Zhou, H. Wu, C. H. He, S. Li, R. Krishna, J. P. Li, W. Zhou, B. L. Chen, *Nat. Mater.* **2018**, *17*, 1128.
[19] V. I. Nikolayenko, D. C. Castell, D. Sensharma, M. Shivanna, L. Loots, K. A. Forrest, C. J. Solanilla-Salinas, K. I. Otake, S. Kitagawa, L. J. Barbour, B. Space, M. J. Zaworotko, *Nat. Chem.* **2023**, *15*, 542.
[20] Z. Chang, D. H. Yang, J. Xu, T. L. Hu, X. H. Bu, *Adv. Mater.* **2015**, *27*, 5432.
[21] B. Le Ouay, S. Kitagawa, T. Uemura, *J. Am. Chem. Soc.* **2017**, *139*, 7886.
[22] G. K. Angeli, E. Loukopoulos, K. Kouvidis, A. Bosveli, C. Tsangarakis, E. Tylianakis, G. Froudakis, P. N. Trikalitis, *J. Am. Chem. Soc.* **2021**, *143*, 10250.
[23] H. Wang, M. Warren, J. Jagiello, S. Jensen, S. K. Ghose, K. Tan, L. Yu, T. J. Emge, T. Thonhauser, J. Li, *J. Am. Chem. Soc.* **2020**, *142*, 20088.
[24] R. B. Lin, L. B. Li, H. Wu, H. Arman, B. Li, R. G. Lin, W. Zhou, B. L. Chen, *J. Am. Chem. Soc.* **2017**, *139*, 8022.
[25] C. M. McGuirk, T. Runcevski, J. Oktawiec, A. Turkiewicz, M. K. Taylor, J. R. Long, *J. Am. Chem. Soc.* **2018**, *140*, 15924.
[26] J. A. Mason, J. Oktawiec, M. K. Taylor, M. R. Hudson, J. Rodriguez, J. E. Bachman, M. I. Gonzalez, A. Cervellino, A. Guagliardi, C. M. Brown, P. L. Llewellyn, N. Masciocchi, J. R. Long, *Nature* **2015**, *527*, 357.
[27] Y. Huang, J. Wan, T. Pan, K. Ge, Y. Guo, J. Duan, J. Bai, W. Jin, S. Kitagawa, *J. Am. Chem. Soc.* **2023**, *145*, 24425.
[28] H. L. Zhou, Y. B. Zhang, J. P. Zhang, X. M. Chen, *Nat. Commun.* **2015**, *6*, 6917.

[29] H. Sato, W. Kosaka, R. Matsuda, A. Hori, Y. Hijikata, R. V. Belosludov, S. Sakaki, M. Takata, S. Kitagawa, *Science* **2014**, *343*, 167.
[30] S. Horike, S. Shimomura, S. Kitagawa, *Nat. Chem.* **2009**, *1*, 695.
[31] S. Q. Ma, D. F. Sun, X. S. Wang, H. C. Zhou, *Angew. Chem. Int. Ed.* **2007**, *46*, 2458.
[32] J. D. Pang, S. Yuan, D. Y. Du, C. Lollar, L. L. Zhang, M. Y. Wu, D. Q. Yuan, H. C. Zhou, M. C. Hong, *Angew. Chem. Int. Ed.* **2017**, *56*, 14622.
[33] Q. Dong, Y. Huang, J. Wan, Z. Lu, Z. Wang, C. Gu, J. Duan, J. Bai, *J. Am. Chem. Soc.* **2023**, *145*, 8043.
[34] Q. Dong, X. Zhang, S. Liu, R. B. Lin, Y. Guo, Y. Ma, A. Yonezu, R. Krishna, G. Liu, J. Duan, R. Matsuda, W. Jin, B. Chen, *Angew. Chem. Int. Ed.* **2020**, *59*, 22756.
[35] Deposition numbers 2266630 (for NTU-88α), 2266631 (for NTU-88o-C_3H_4), 2266632 (for NTU-88c), 2266633 (for NTU-88β) and 2266634 (for NTU-88 as synthesized) contain the supplementary crystallographic data for this paper. These data are provided free of charge by the joint Cambridge Crystallographic Data Centre and Fachinformationszentrum Karlsruhe Access Structures service.

Manuscript received: November 5, 2023
Accepted manuscript online: November 13, 2023
Version of record online: November 27, 2023

Angewandte Chemie
Eine Zeitschrift der Gesellschaft Deutscher Chemiker

Supporting Information

Molecular Sieving of Propyne/Propylene by a Scalable Nanoporous Crystal with Confined Rotational Shutters

*J. Wan, H.-L. Zhou, K. Hyeon-Deuk, I-Y. Chang, Y. Huang, R. Krishna, J. Duan**

Materials and Methods

All reagents and solvents were commercially available and used as received.

Synthesis of Ligand. The ligand was synthesized according to the previously report.[1]

Small-scale synthesis of $[Ni(L)_2Cl_2]\cdot x$Solvent (NTU-88). Synthesis of **NTU-88** was accomplished by mixing the ligand (**L**: 4,4'-dipyridylnitride) (4 mg, 0.023 mmol) and $NiCl_2\cdot 6H_2O$ (8 mg, 0.034 mmol) in a solution of *N,N*'-dimethylformamide (DMF)/EtOH/H_2O (3/1/0.25, 4.25 mL) in a container. After heating this solution at 353 K for 1 day, light green diamond-shaped crystals can be harvested by washing them with DMF (Yield: ~40.0% based on **L**).

Large-scale synthesis of NTU-88. After mixing **L** (24.5 g, 142.3 mmol) and $NiCl_2\cdot 6H_2O$ (41.7 g, 193.8 mmol) in solvents of DMF/EtOH/H_2O (3/1/0.25, v/v/v, total: 900 mL), ammonia (4.5 mL) was added into the above strongly stirred solution at room temperature. Within 1 minute, a large amount of green microcrystals appeared. Totally, about 60 g sample was obtained after filtration, washing and air-drying (Yield: ~90.0% based on **L**).

Fourier-transform Infrared (FT-IR) spectra. FT-IR were recorded from KBr pellets in the range of 4000–500 cm^{-1} on a VECTOR 22 spectrometer.

Thermogravimetric analyses. TG analysis were performed using a STA 209 F1 (NETZSCH Instruments) thermo-microbalance, heating from room temperature to 650°C at a rate of 10°C min^{-1} under nitrogen flow.

Single-crystal X-ray diffraction measurements. Data collection and structural analysis of the crystals were collected on a Bruker Smart Apex CCD diffractometer at 298 K using graphite monochromator Mo/Kα radiation (λ = 0.71073 Å). The data was reduced using the Bruker Saint program. The structures were solved using direct methods and refined using the full-matrix least squares technique with the SHELXTL package.[2] Organic hydrogen atoms were placed in calculated positions with isotropic displacement parameters set to 1.2 × Ueq of the attached atom.

Powder X-Ray Diffraction (PXRD) pattern. PXRD were tested with Bruker AXS D8 Advance (test conditions: 40 kV, 40 mA, CuKα, λ = 1.5418 Å, scanning range 5-40°). Simulated powder patterns were generated from single-crystal X-ray diffraction data using Mercury 1.4.2 software.

In-situ powder X-ray diffraction (PXRD) measurements. After loading the initial activated **NTU-88** into the sample cell, the crystals were then activated under dynamic vacuum at 373 K for 20 h. After cooling down, PXRD patterns were collected under varied pressure of C_3H_4 or C_3H_6 at 298 K, with pressure being maintained by a highly sensitive regulator.

Structural refinements. PXRD data for Pawley refinements were collected using a Rigaku X-ray powder diffractometer (Cu Kα) at 298 K with a scanning speed of 2°/step. Indexing and Pawley refinements of the PXRD patterns were carried out by using the Reflex module of Material Studio 7.0. The patterns were indexed by the X-cell method. The space groups were identified with well acceptable FOM values.

To enture good agreement between the calculated and the experimental patterns, the peak profiles, zero-shift, background, and unit-cell parameters were refined step by step. The peak profiles were refined by the Pseudo-Voigt function with Berar-Baldinozzi asymmetry correction parameters. The structure models were built by using the Crystal Building module, utilizing the space groups and unit-cell parameters obtained from the Pawley refinements, and then optimized by the *Forcite* module using the universal force field.

Sample activation. To activate the crystals, the as-synthesized **NTU-88** was soaked in dry methanol for 3 days. During these, the leaching solution was exchanged with fresh methanol for every 8 hours. The crystals were then evacuated at room temperature for 6 h, 333 K for 2 h and 373 K for 20 h under a dynamic vacuum.

Single-gas sorption measurements. Gas sorption measurements were performed on a Belsorp volumetric adsorption instrument (BEL Japan Corp.). In the sorption measurements, ultra-high-purity grade gases of C_3H_4, C_3H_6, N_2 and CO_2 were used throughout the adsorption experiments.

Breakthrough measurements. The initial activated samples (3.05 g) were tightly packed into a stainless-steel column (φ = 0.30 cm, *L* = 20 cm). Then, the column was activated under vacuum at corresponding temperature and then swept with N_2 flow to remove impurities. Until no any signal was detected, the gas flow was dosed into the column. Breakpoints were determined by gas chromatography. Between cycling experiments, re-generation can be achieved by vacuuming at 373 K for half hour. Pressure of feed gas is 1 bar.

Estimation of the isosteric heats of gas adsorption. The unary isotherm data for C_3H_4 measured at three different temperatures (283 K, 298 K, and 308 K) in NTU-88 were fitted with excellent accuracy using the dual-site Langmuir-Freundlich model, where we distinguish two distinct adsorption sites A and B:

$$q = \frac{q_{sat,A} b_A p^{\nu A}}{1 + b_A p^{\nu A}} + \frac{q_{sat,B} b_B p^{\nu B}}{1 + b_B p^{\nu B}} \tag{S1}$$

In eq (S1), the Langmuir-Freundlich parameters b_A, b_B are both temperature dependent

$$b_A = b_{A0} \exp\left(\frac{E_A}{RT}\right); \quad b_b = b_{B0} \exp\left(\frac{E_B}{RT}\right) \tag{S2}$$

In eq (S2), E_A, E_B are the energy parameters associated with sites A, and B, respectively.

The unary isotherm data for C_3H_6 measured at three different temperatures (283 K, 298 K, and 308 K) in **NTU-88** were fitted with excellent accuracy using the single-site Langmuir model. The fit parameters are provided in Table S.

The isosteric heat of adsorption, Q_{st}, is defined as

$$Q_{st} = -RT^2 \left(\frac{\partial \ln p}{\partial T}\right)_q \tag{S3}$$

where the derivative in the right member of eq (S3) is determined at constant adsorbate loading, q. The derivative was determined by analytic differentiation of the combination of eq (S1), eq (S2), and eq (S3). This procedure has been used also previously for calculation of Q_{st} for the flexible PCPs.[3]

Ab initio computations. All the density functional theory (DFT) computations were performed with the Becke, three-parameter, Lee-Yang-Parr (B3LYP) functional in the Gaussian 09 package.[4] Unless otherwise mentioned, the basis set is 6-31G (d,p). The unit structures of **NTU-88c** and **NTU-88o** were extracted from the bulk crystal structures. The aromatic side-chains outside the gas channels were replaced by H atoms. Then, the XYZ coordinates of all the H atoms were optimized with all the heavy-atom coordinates being fixed. The structures of C_3H_4 and C_3H_6 molecules were fully optimized without any constraint with 6-311G (d,p) basis set.

The static pore size of **NTU-88c** and **NTU-88o** as well as the static cross sections of C_3H_4 and C_3H_6 were estimated using their electronic density surfaces. The three-dimensional (3D) electronic density surface was obtained through the following steps: (1) The electronic density was calculated from the converged wave function computed with the 6-311G(d,p) basis set using the utility cubegen program of Gaussian 09 package. (2) The 3D electronic density surface was visualized using the VESTA package[5] with an isovalue of 0.002. As shown in Fig 4a-4b, the electronic density surfaces of C_3H_4 and C_3H_6 almost coincide with their molecular surface formed by the atomic spheres with the van der Waal's radii of all the composing atoms. The narrowest and broadest static pore size of **NTU-88c** and **NTU-88o** are shown in Figs. S18 and S19, respectively. The narrowest pores stem from the largest steric hindrance to the gas channel from the pyridine sidechains while the broadest pores are less affected by the pyridine sidechains.

The pyridine sidechains existing along the channels are almost freely rotating around their rotational axes at ambient temperature. The red-dashed lines in Fig.S20 represent the rotational axes of the pyridine sidechains. The atoms located along the rotational axes do not change while the pyridine sidechains are rotating and thus determine the dynamical pore size of the channel in **NTU-88c** and **NTU-88o**. The dynamical pores of **NTU-88c** and **NTU-88o** are shown in Figs.4e-4f were made by excluding the influence of the rotating pyridine sidechains that is by removing the atoms outside the pyridine rotational axes, marked by the yellow-colored shadows in Fig. S19. The resulting surface formed by the van der Waal's radii of the atoms composing the channels in the dynamical pores are shown in Figs. 4e-4f.

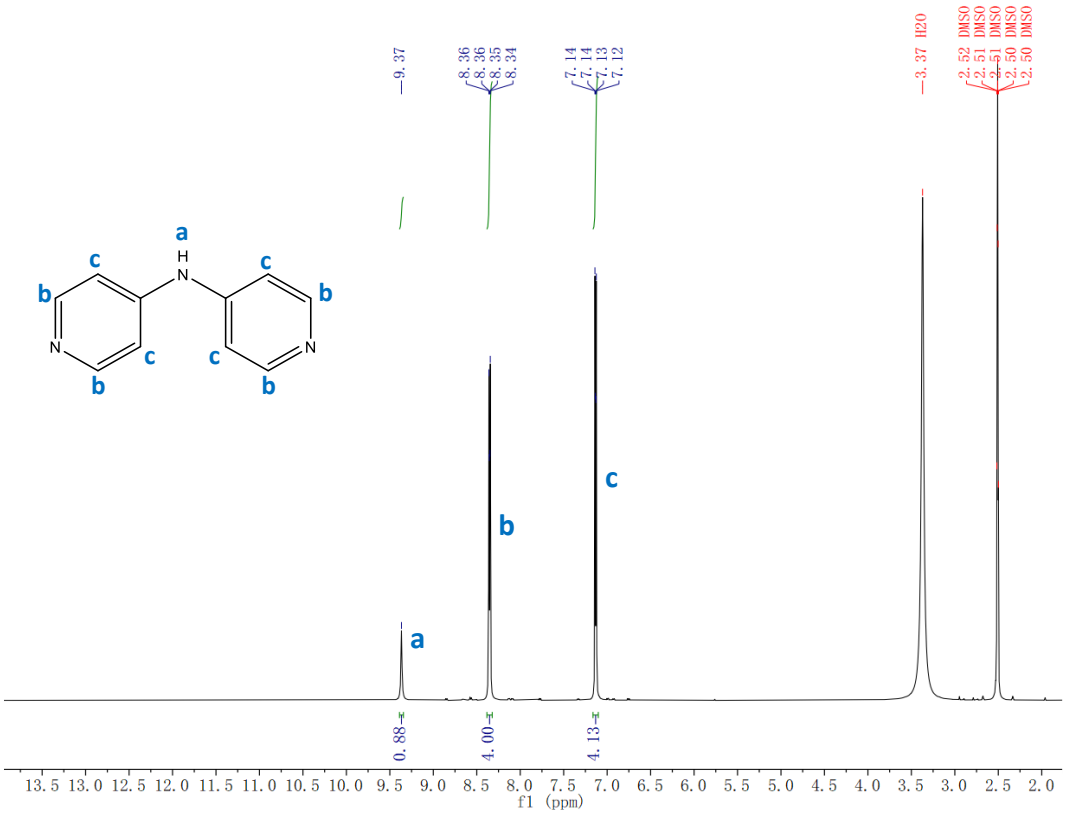

Figure S1. ^{1}HNMR spectrum of the ligand.

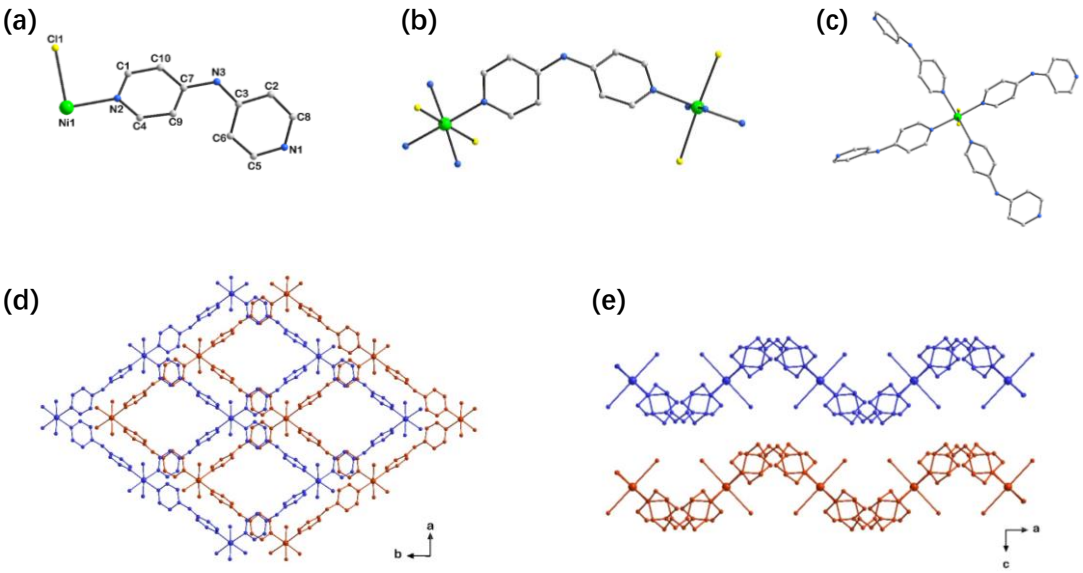

Figure S2. Structural view of **NTU-88**: (a) Asymmetric unit; (b) ligand connection; (c) Ni^{2+} connection; 2D layered structure along *c* axis (d) and *b* axis (e).

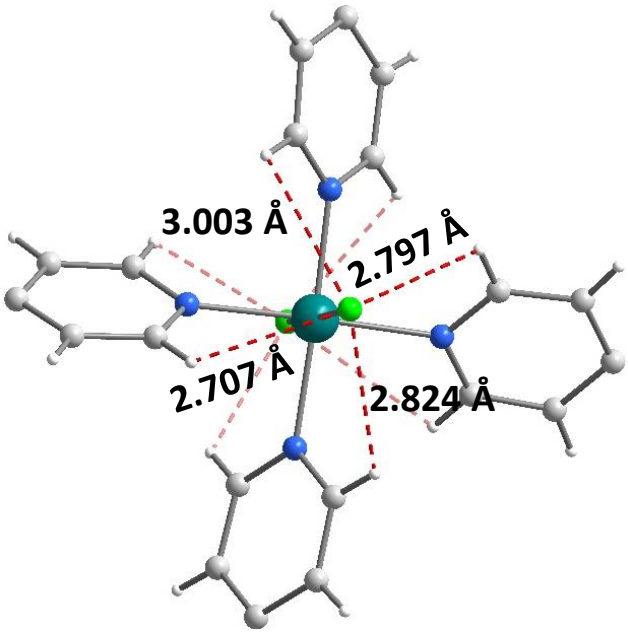

Figure S3. View of the formed halogen bonds between Cl^- and four pyridine rings.

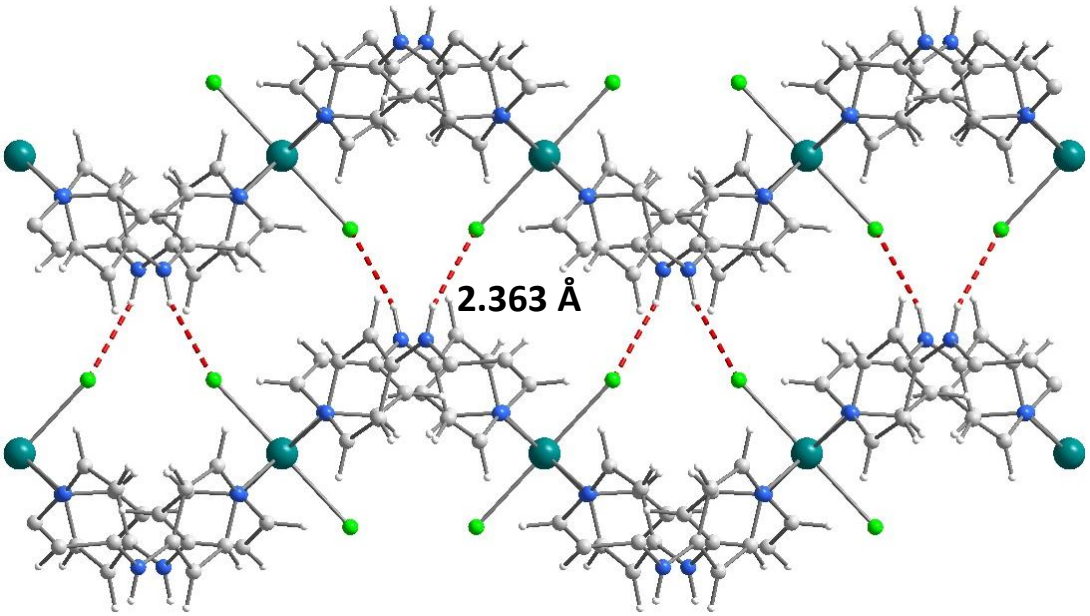

Figure S4. View of the formed halogen bonds between adjacent interlayers.

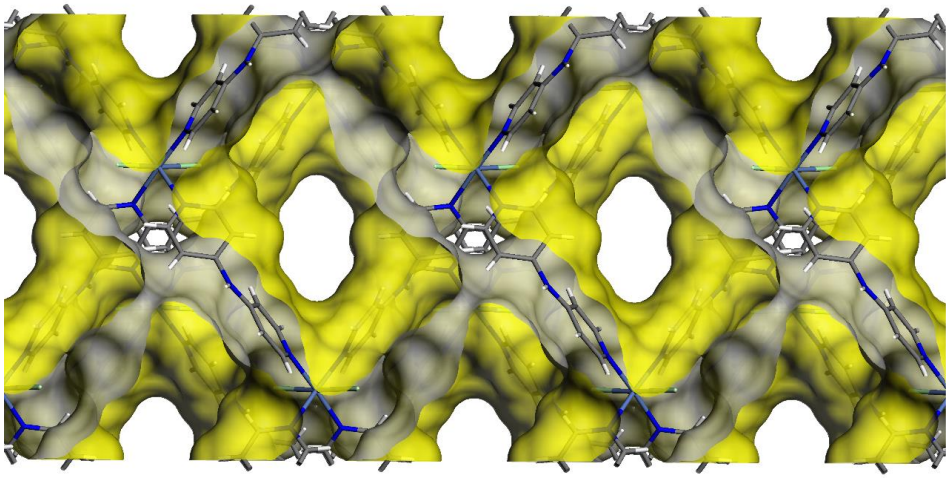

Figure S5. View of the accessible inner surface of **NTU-88**.

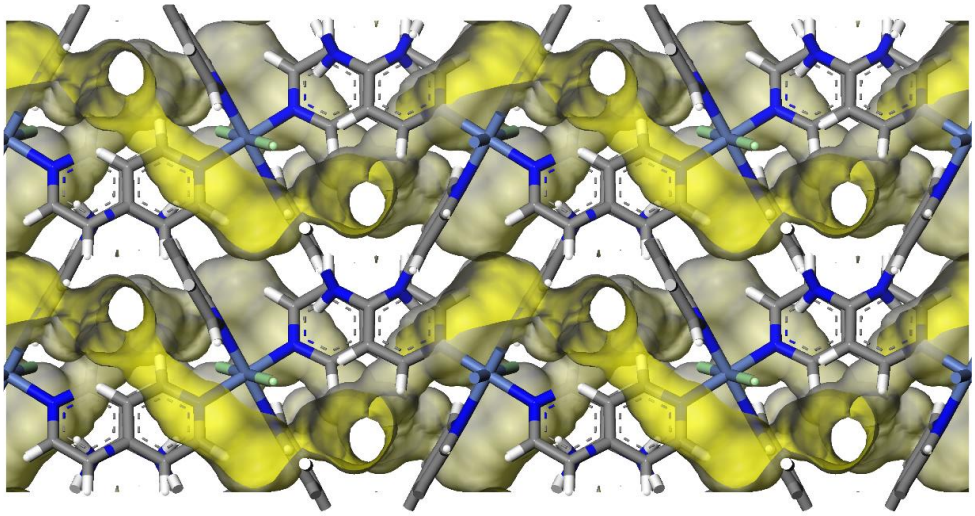

Figure S6. View of the accessible inner surface of **NTU-88c**.

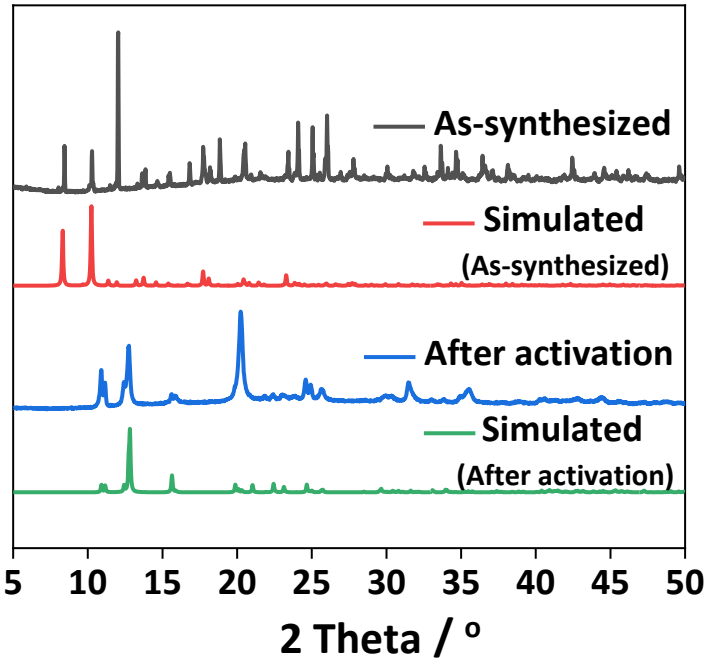

Figure S7. PXRD of **NTU-88** for synthesized and activated samples.

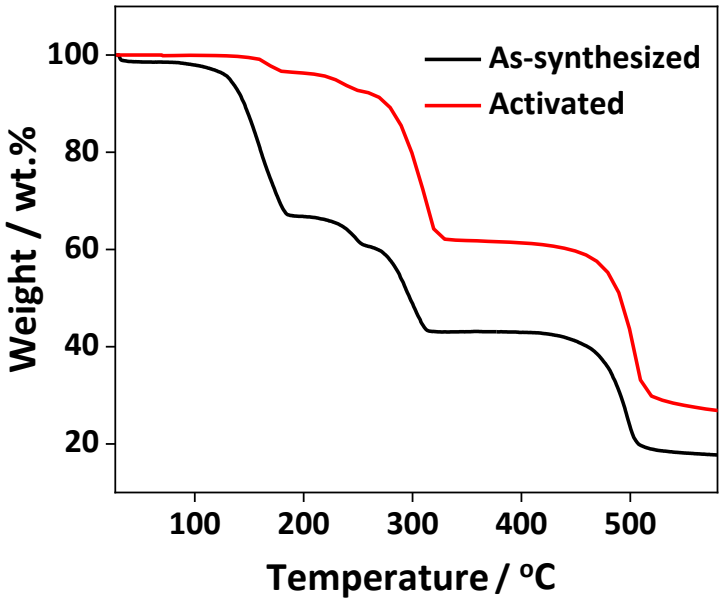

Figure S8. TG of **NTU-88**.

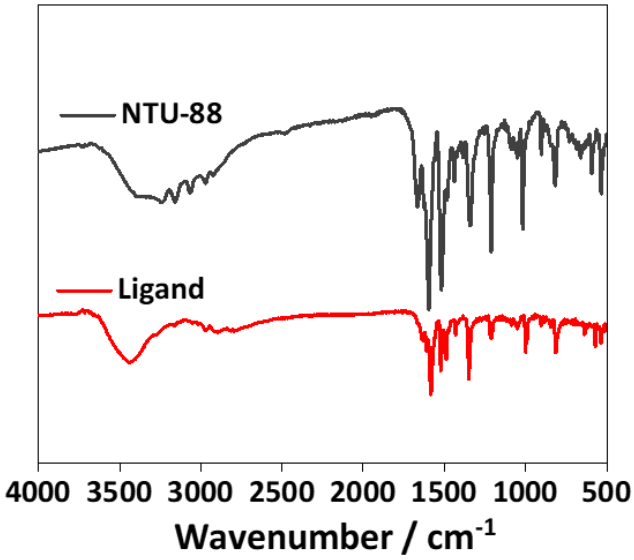

Figure S9. IR of **NTU-88** and the ligand.

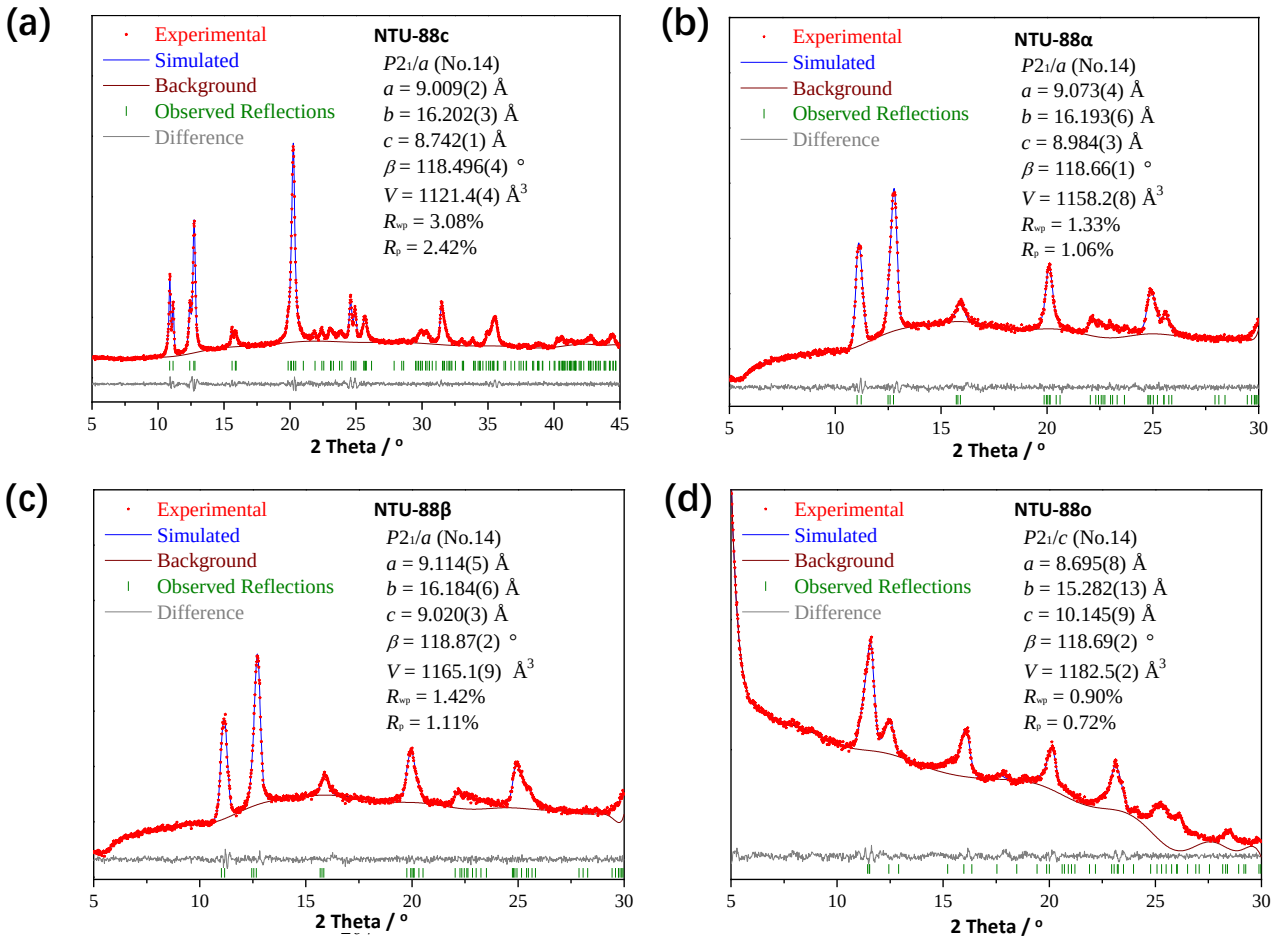

Figure S10. Pawley refinements of **NTU-88** at different states.

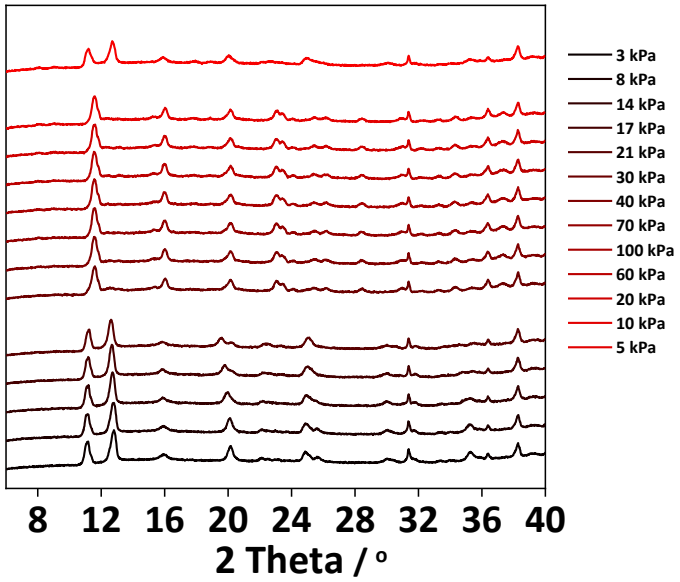

Figure S11. The in-situ XRD of **NTU-88c** at 298K under C_3H_4 atmosphere.

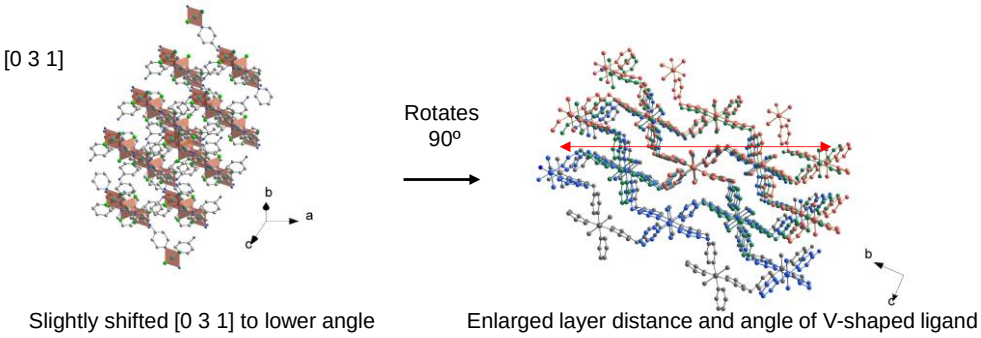

Figure S12. View of the structure along [0 3 1] plane in **NTU-88c** and corresponding view after rotation of 90 º.

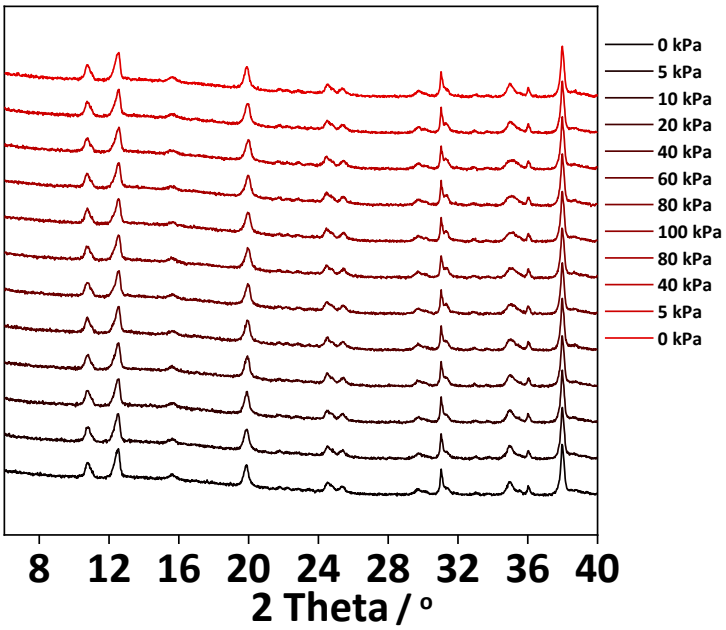

Figure S13. The in-situ XRD of **NTU-88c** at 298K under C_3H_6 atmosphere.

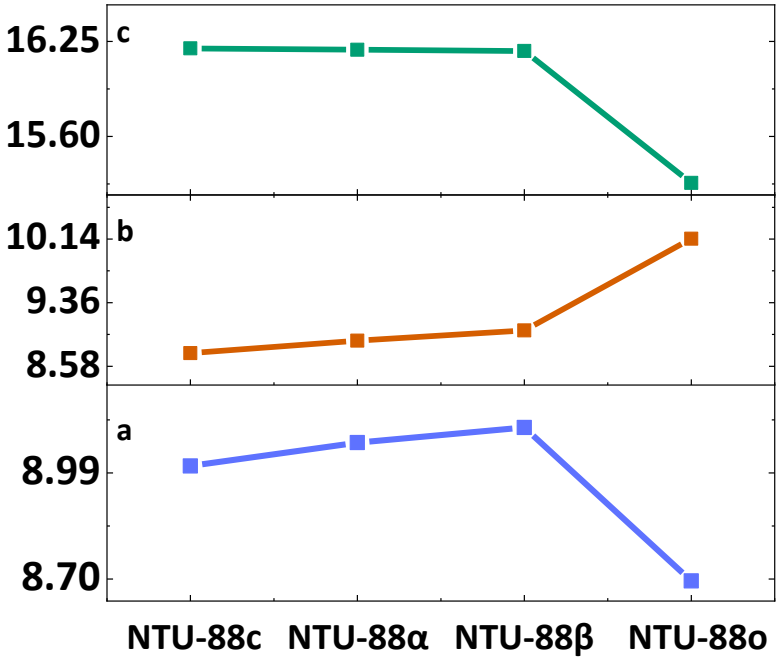

Figure S14. Side length of the unit cell of **NTU-88c**, **NTU-88α**, **NTU-88β** and **NTU-88o**.

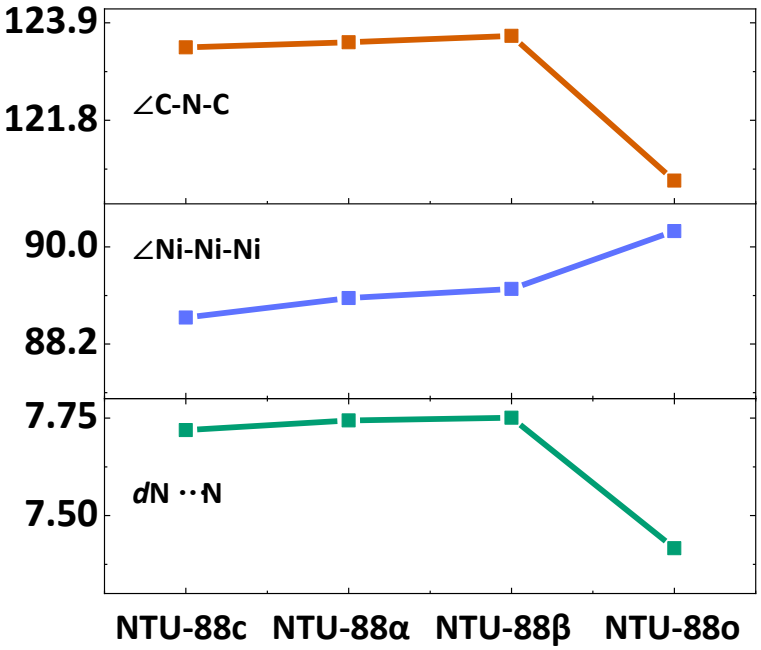

Figure S15. Variation of the involved angle (°) and distance (Å) in **NTU-88c**, **NTU-88α**, **NTU-88β** and **NTU-88o**.

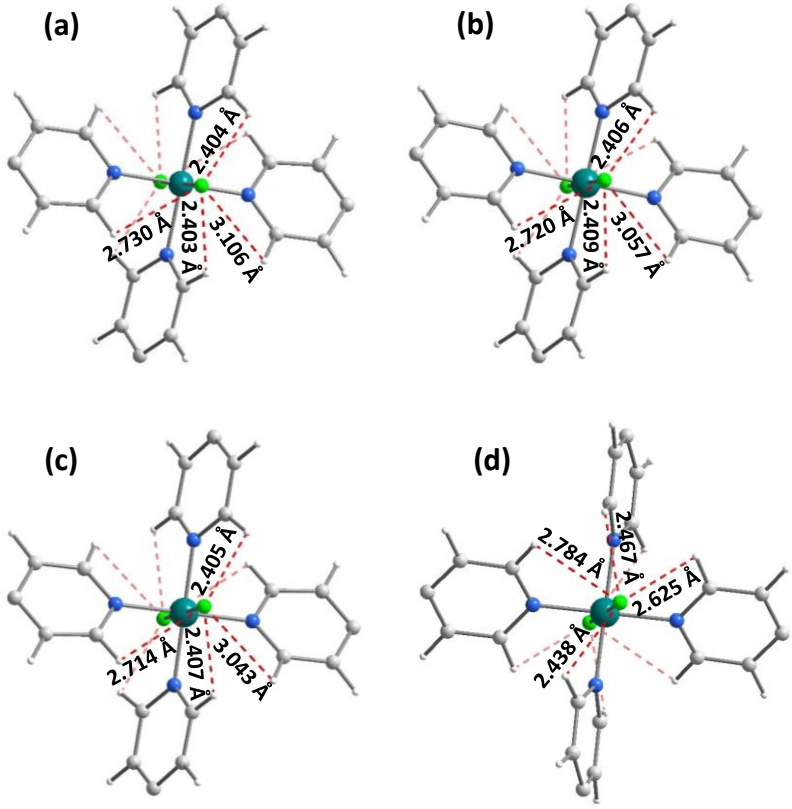

Figure S16. View of the halogen bonds between Cl^- and four pyridine rings in **NTU-88c**, **NTU-88α**, **NTU-88β** and **NTU-88o**.

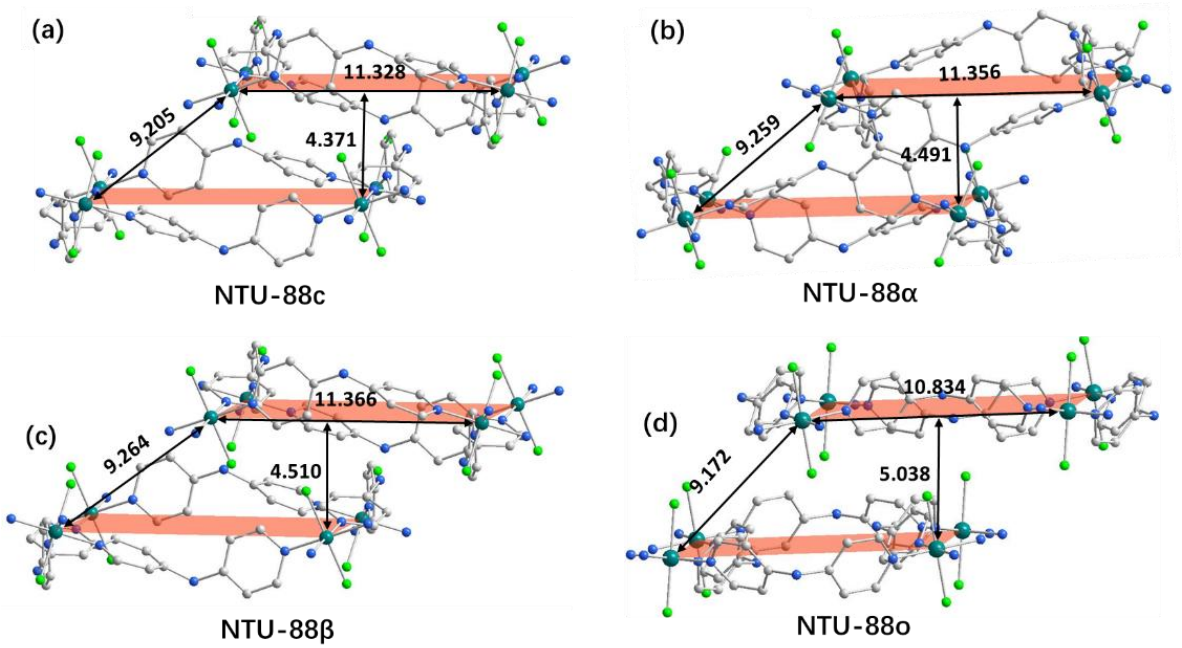

Figure S17. View of the distance between the adjacent layers in **NTU-88c**, **NTU-88α**, **NTU-88β** and **NTU-88o**. Unit for distance is Å.

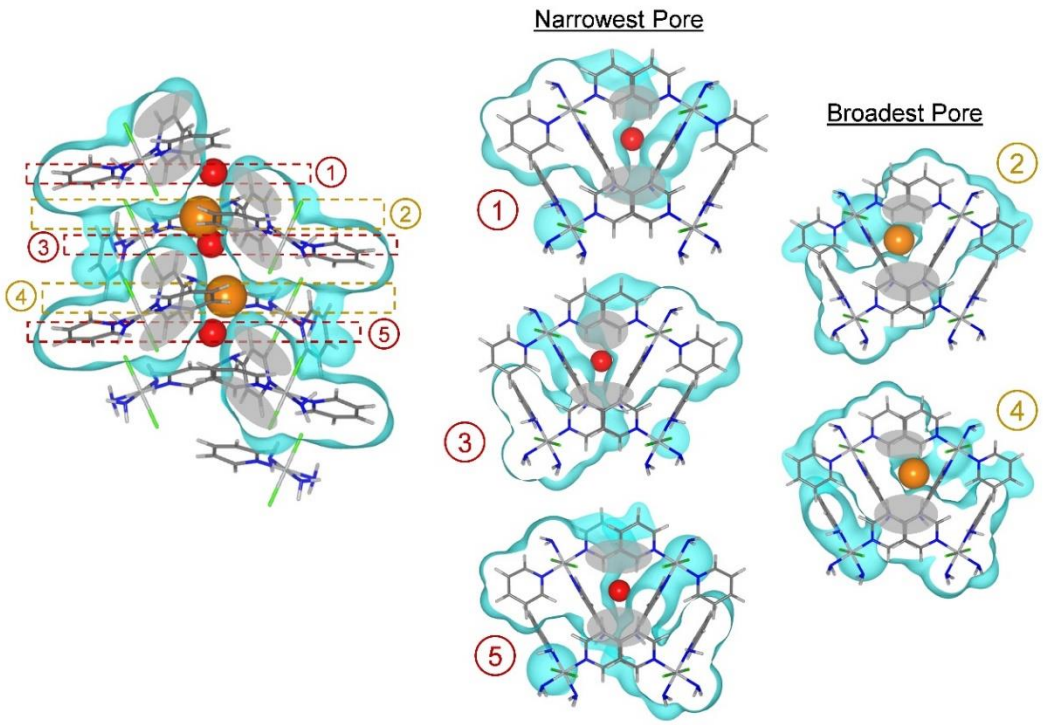

Figure S18. Static pore size of the gas channel in **NTU-88c**. Five cross sections possessing the narrowest and broadest steric pores are cut and shown with the red and orange balls whose diameters are 1.6 Å and 2.4 Å, respectively.

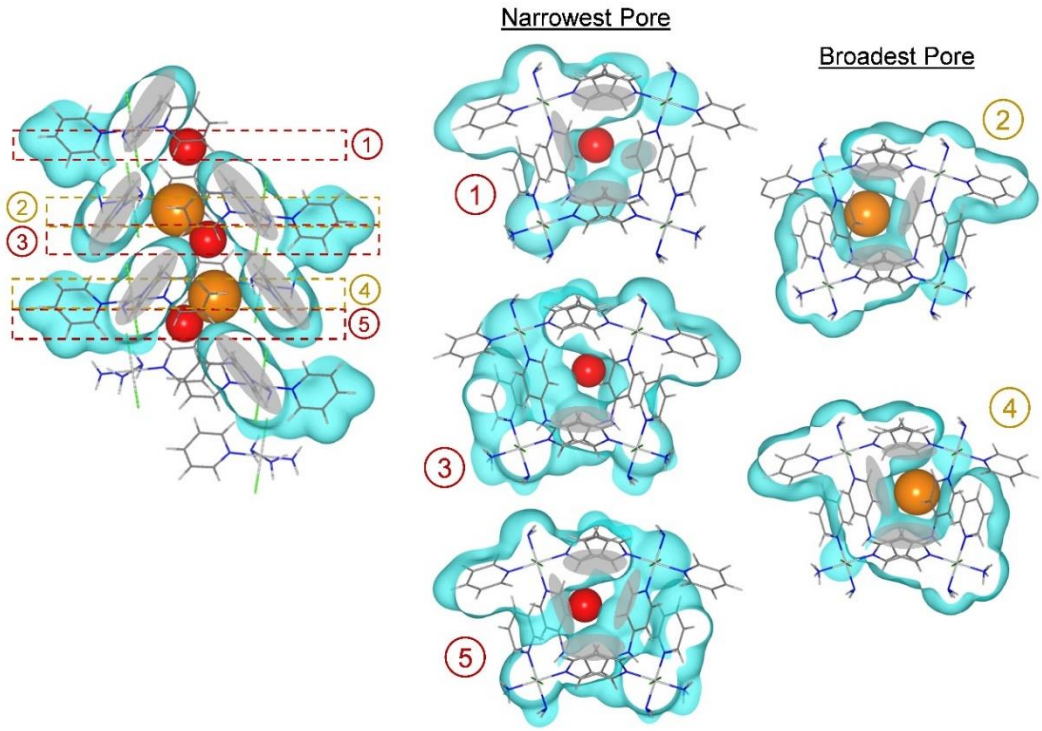

Figure S19. Static pore size of the gas channel in **NTU-88o**. Five cross sections possessing the narrowest and broadest steric pores are cut and shown with the red and orange balls whose diameters are 2.5 Å and 3.2 Å, respectively.

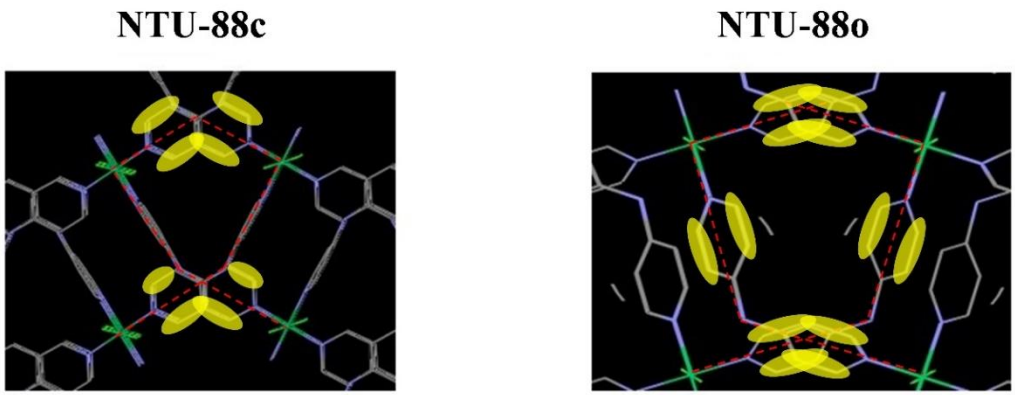

Figure S20. Rotational axes of the pyridine sidechains (red-dashed lines) used to make the dynamical pores of **NTU-88c** and **NTU-88o** shown in Figs.4e-4f.

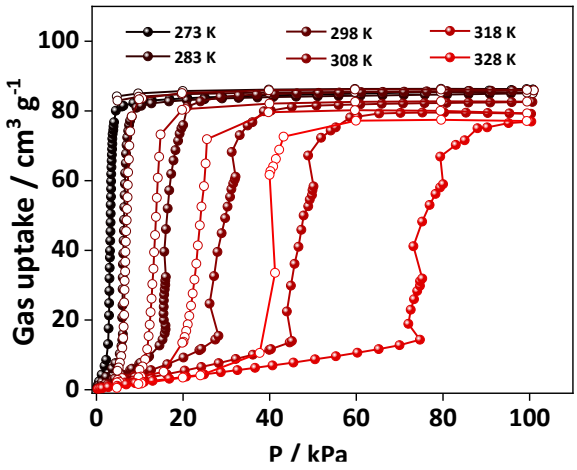

Figure S21. C_3H_4 adsorption isotherms of **NTU-88** at different temperatures. The sudden pressure drop for the isotherms at 298-328 K is related to the fast gate-opening process and retention of the open state. At gate-opening pressure, the framework change to open state which adsorbed large amount of gas and lead to a pressure drop. While the **NTU-88** remains open even the pressure dropped. Such phenomenon is different from the "negative sorption" material reported in Nature 2016, 532, 348, which exhibit lower adsorption amount at higher pressure during the phase transition process.

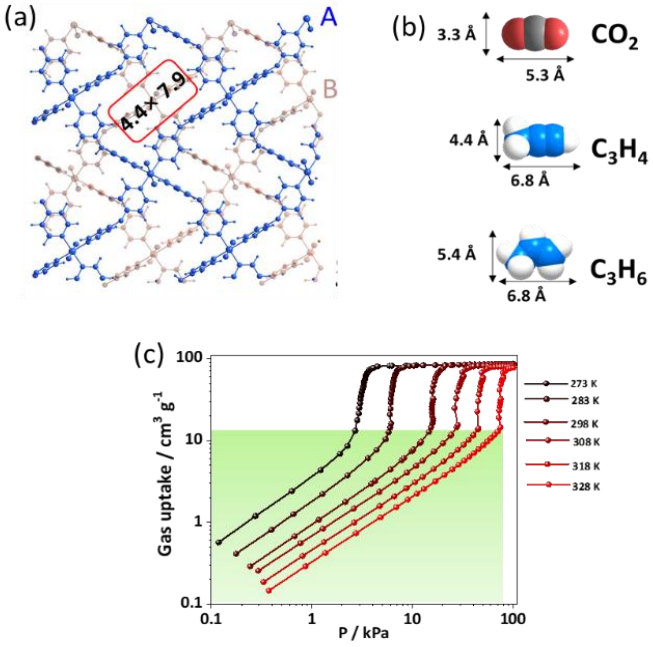

Figure S22. View of the AB stacked layers of **NTU-88** (a) and the molecular dimensions of the gases (b), Plotted C_3H_4 adsorption isotherms at different temperatures in logarithmic form (c). **NTU-88** is a layered (AB) structure. The pore size in A layer is 4.4×7.9 $Å^2$, which is larger than that of the molecular size of CO_2 and C_3H_4, but smaller than that of C_3H_6. Therefore, these single-layered pores allow only about 10 cm^3/g C_3H_4 uptake (lie-down model) before gate-opening, but nearly no C_3H_6 uptake. In addition, the C_3H_4 adsorption linearly increase with increasing pressure, reflecting again the pressure-dependent adsorption in these single-layered pores.

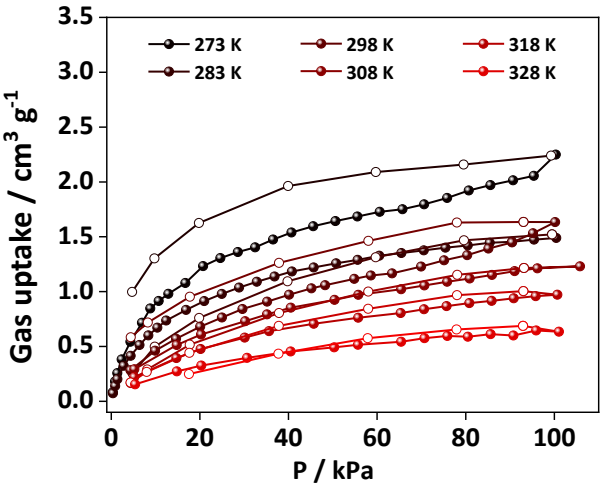

Figure S23. C_3H_6 adsorption isotherms of **NTU-88** at different temperatures.

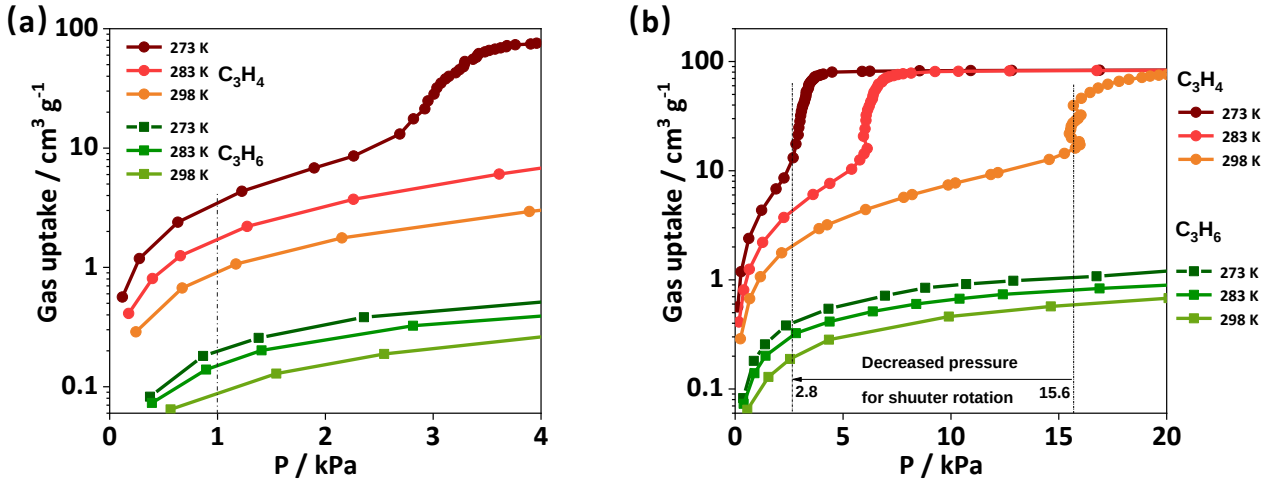

Figure S24. Single-component gas isotherms of **NTU-88** with different scales of X-axes (0-4 kPa: a and 0-20 kPa: b).

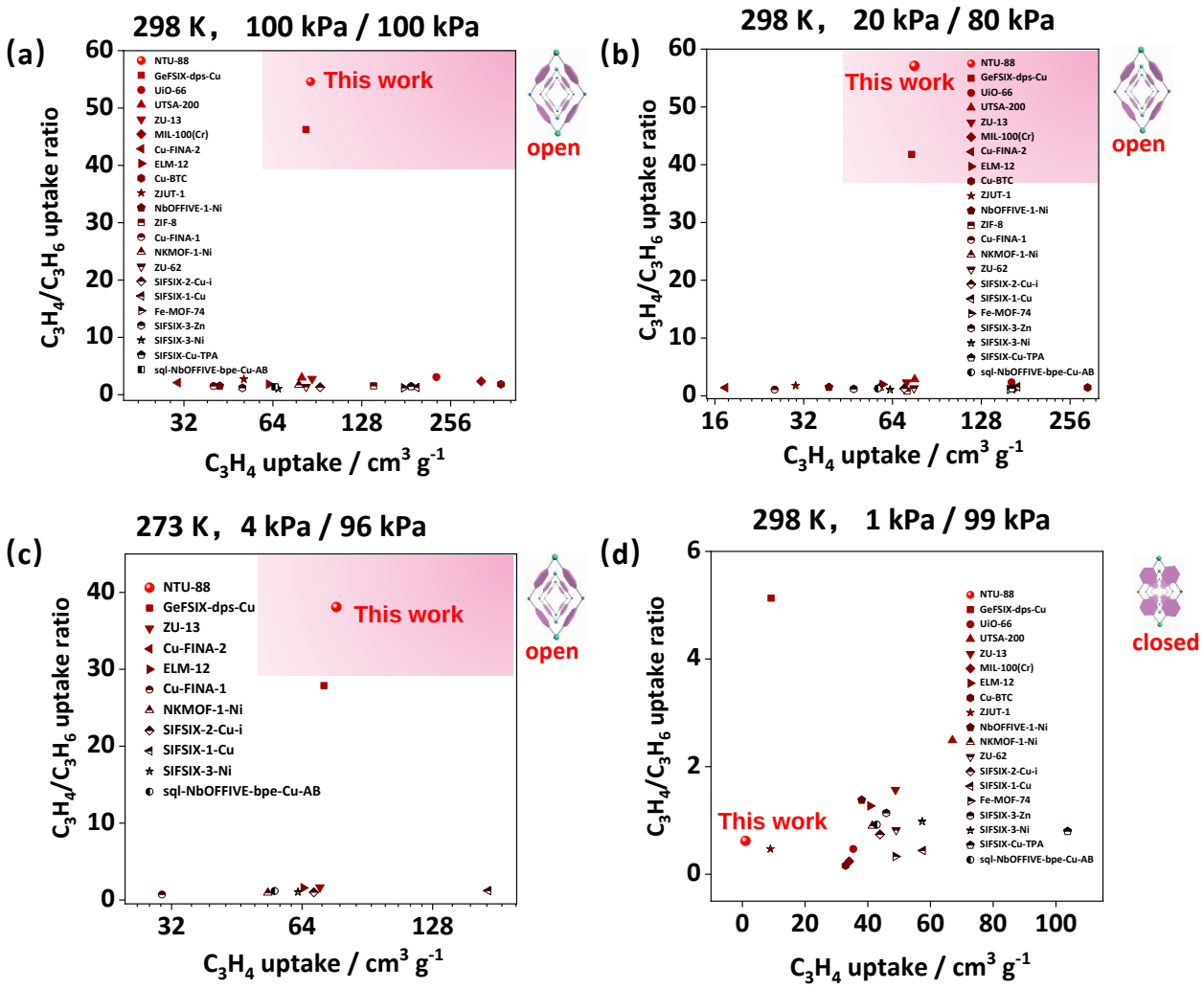

Figure S25. Comparison of C_3H_4/C_3H_6 uptake ratios of between **NTU-88** and other PCPs at different temperature and different partial pressures.

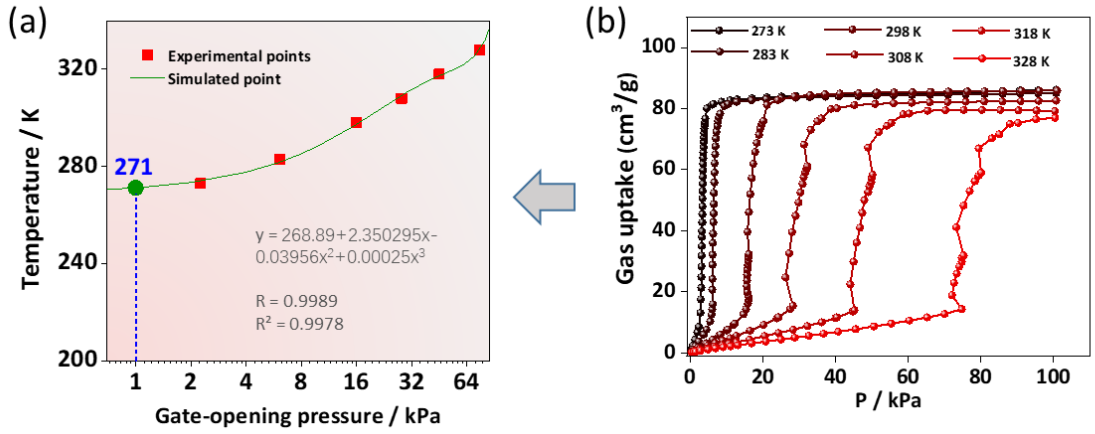

Figure S26. Predicted temperature for shutter rotation in **NTU-88** at 1 kPa (a), according to the C_3H_4 isotherms at different temperature (b).

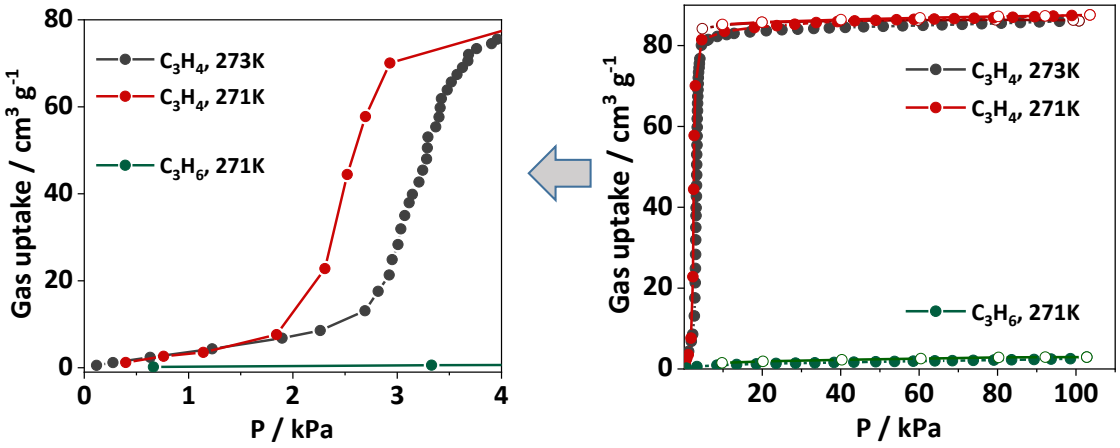

Figure S27. Single-component gas isotherms of C_3H_4 and C_3H_6 of **NTU-88** at 271 K. The C_3H_4 pressure for shutter rotation shows a certain advance, but remains higher than 1 kPa.

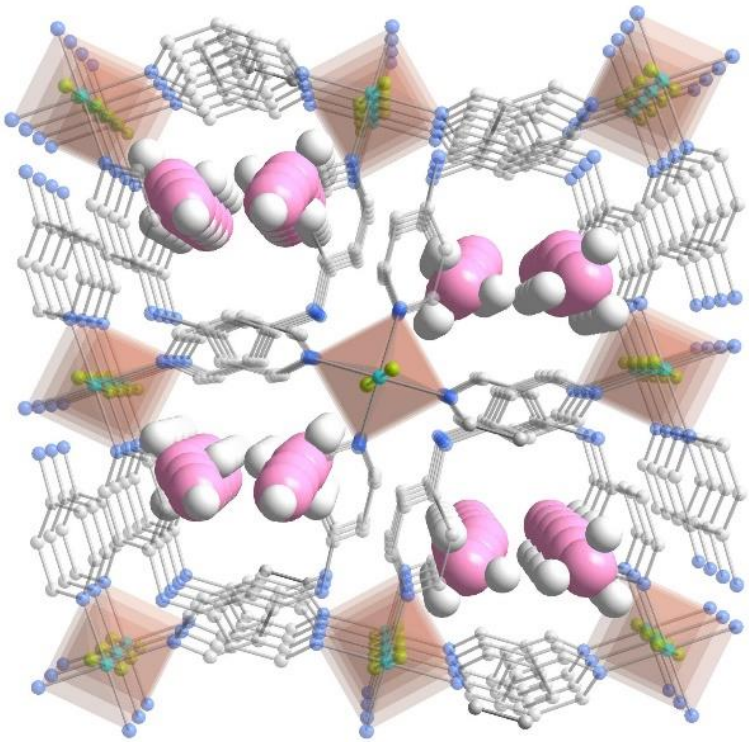

Figure S28. View of the packed C_3H_4 in **NTU-88c** along *c*-axis.

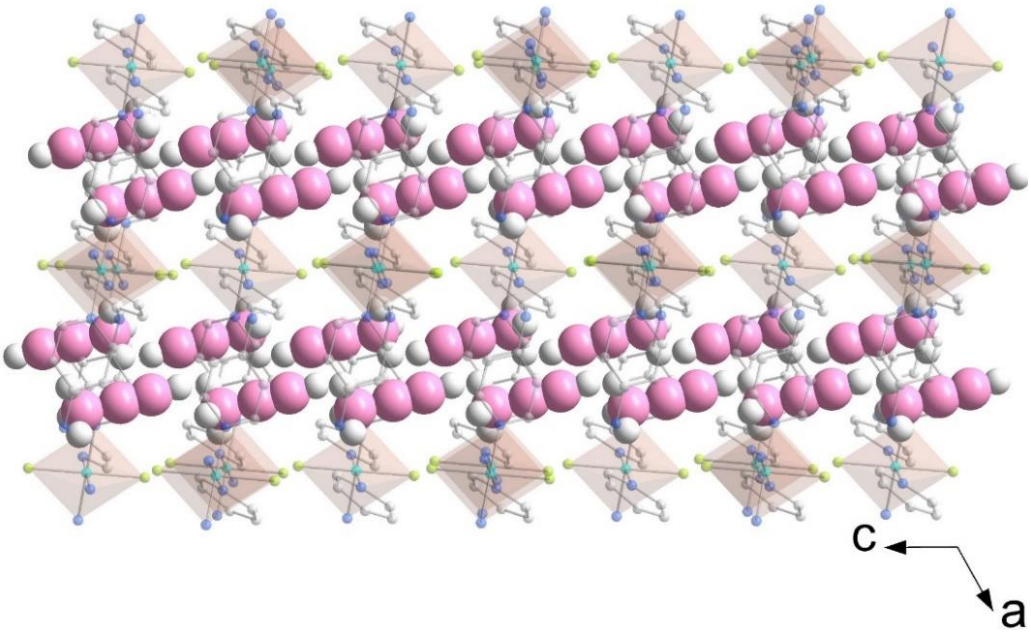

Figure S29. View of the packed C_3H_4 in **NTU-88c** along *b*-axis.

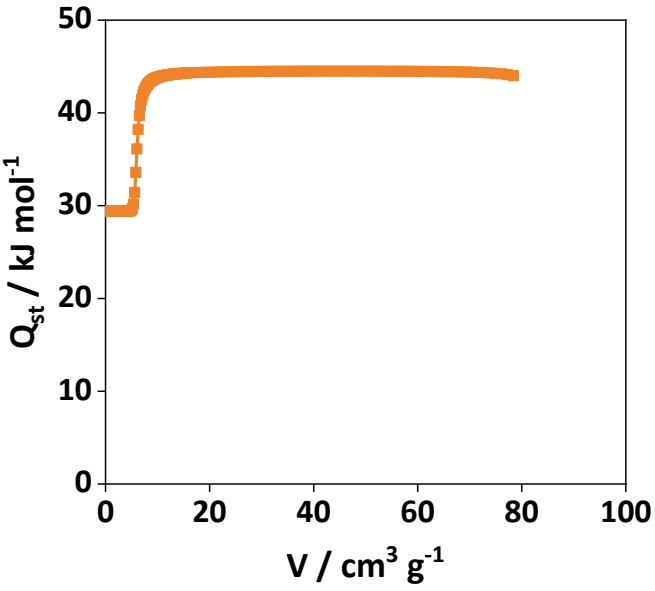

Figure S30. Isosteric heats of adsorption of **NTU-88** for C_3H_4 based on adsorption isotherms at 283, 298 and 308 K.

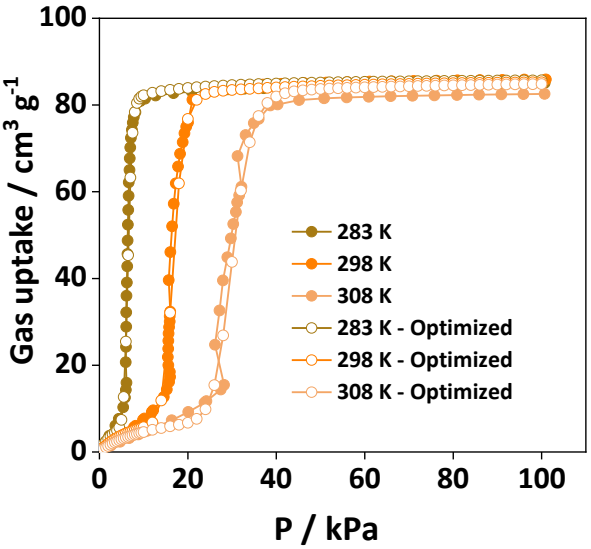

Figure S31. Adsorption isotherms fitting (dual-site Langmuir-Freundlich model) of C_3H_4 at three temperatures in **NTU-88**. The matched isotherms validates excellent accuracy.

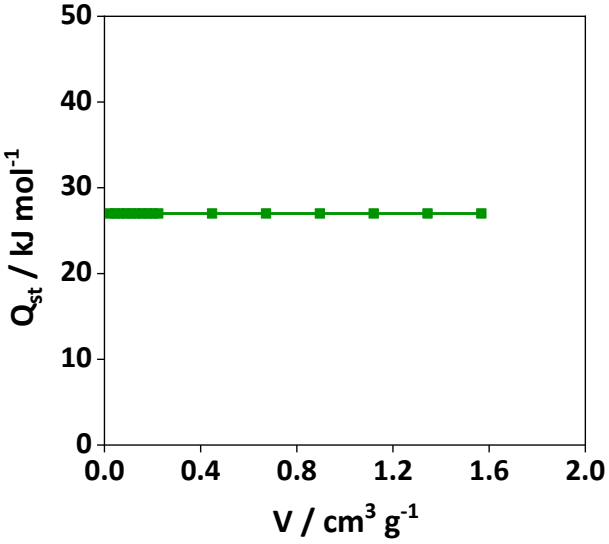

Figure S32. Isosteric heats of adsorption of **NTU-88** for C_3H_6 based on adsorption isotherms at 283, 298 and 308 K.

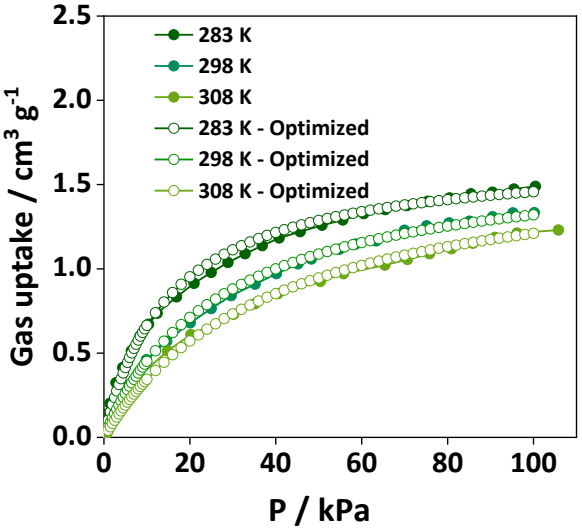

Figure S33. Adsorption isotherms fitting (single-site Langmuir-Freundlich model) of C_3H_6 at three temperatures in **NTU-88**. The matched isotherms validates excellent accuracy.

Figure S34. View of the automatic breakthrough equipment designed and used in our group.

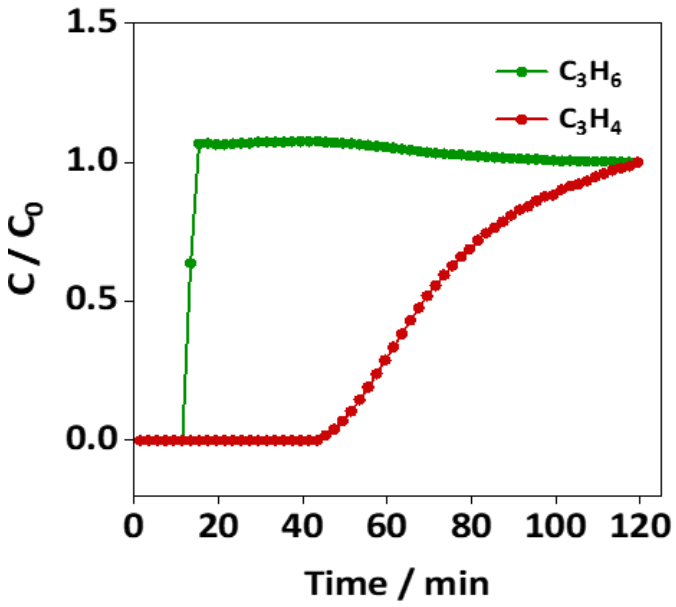

Figure S35. Experimental breakthrough curve of **NTU-88** for C_3H_4/C_3H_6 (10/90, v/v, 2 mL/min) mixture at 298K.

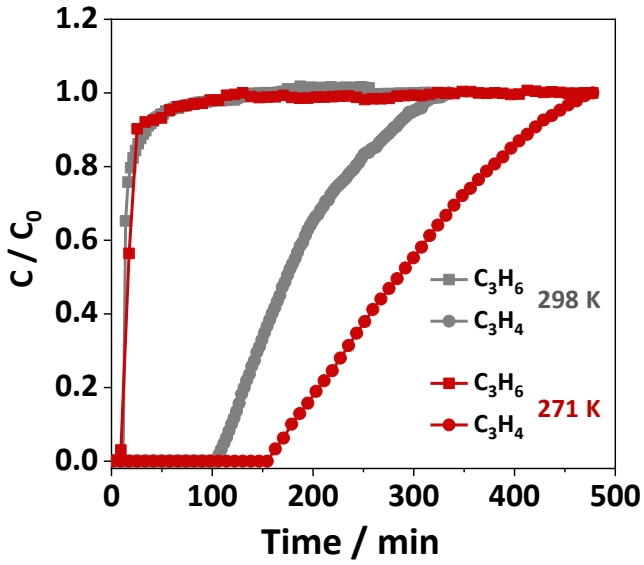

Figure S36. Breakthrough curves of **NTU-88** for C_3H_4/C_3H_6 (1/99, v/v, 2 mL/min) mixture at different temperatures.

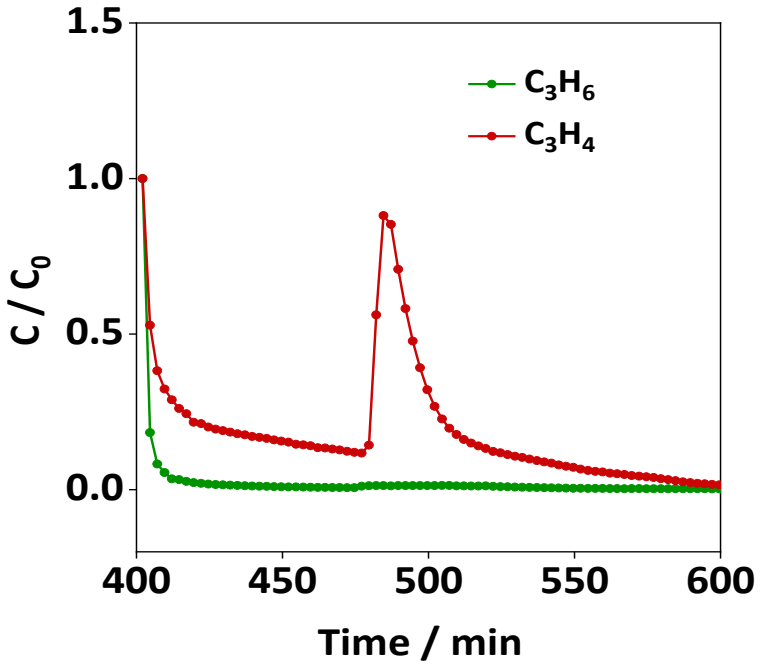

Figure S37. Desorption breakthrough curve of **NTU-88** for C_3H_4/C_3H_6 (1/99, v/v, 5 mL/min) at 298 K. Purity of desorbed C_3H_4 is as high as 99.9%.

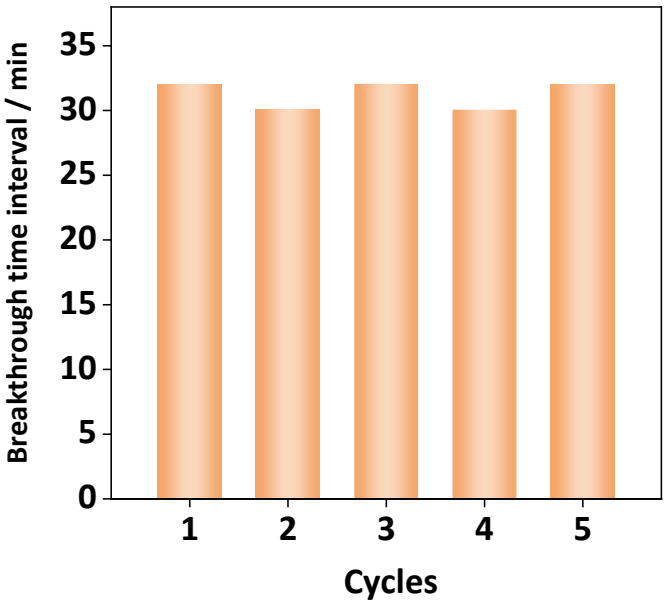

Figure S38. Cycling breakthrough tests of **NTU-88** with feeding gas of C_3H_4/C_3H_6 (10/90, v/v, 2 mL/min) at 298 K.

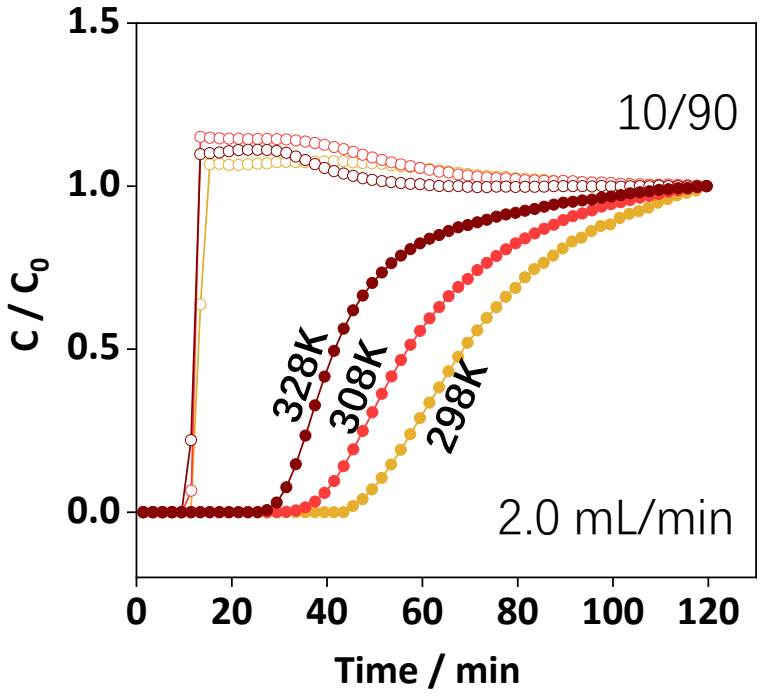

Figure S39. Experimental breakthrough curves of **NTU-88** for C_3H_4/C_3H_6 (10/90, v/v, 2 mL/min) at 298, 308 and 328 K.

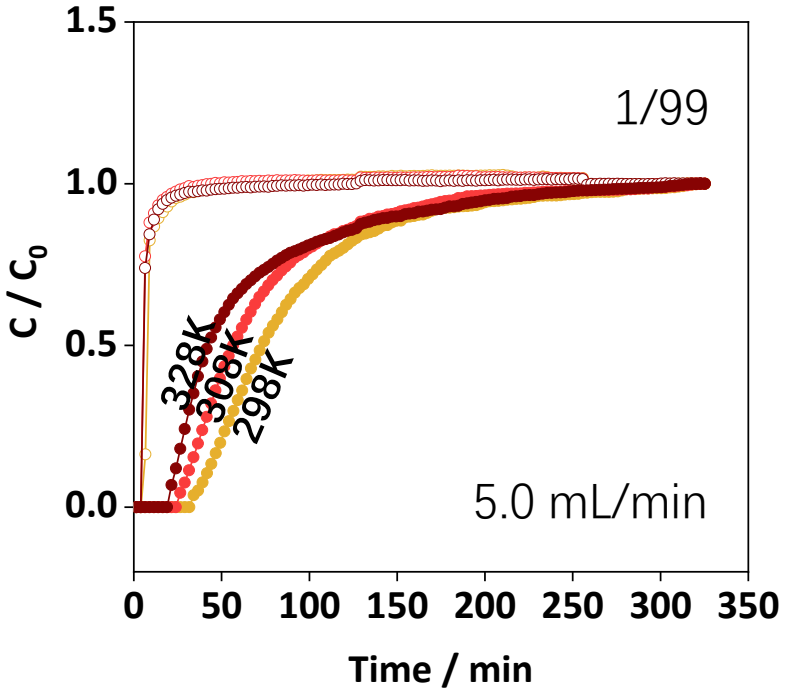

Figure S40. Experimental breakthrough curves of **NTU-88** for C_3H_4/C_3H_6 (1/99, v/v, 5 mL/min) at 298, 308 and 328 K.

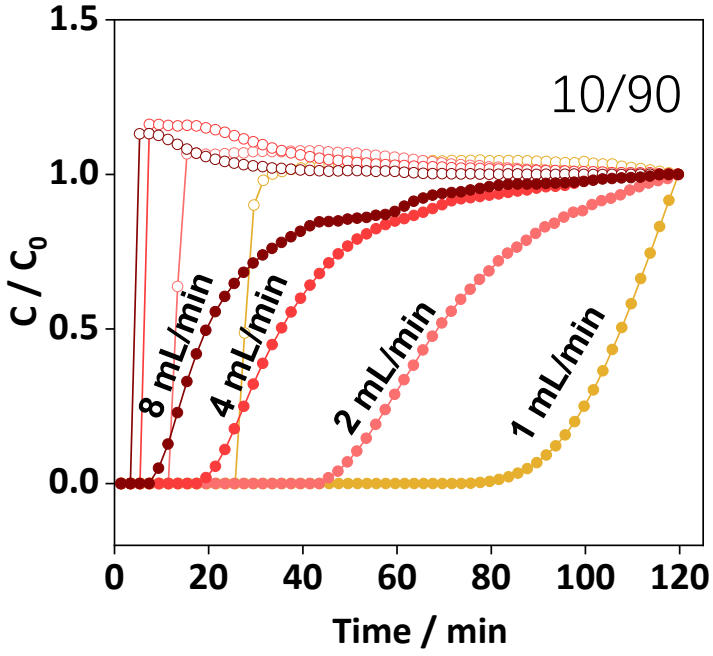

Figure S41. Experimental breakthrough curves of **NTU-88** for C_3H_4/C_3H_6 (10/90, v/v) at 298K with a total flow of 1, 2, 4 and 8 mL/min.

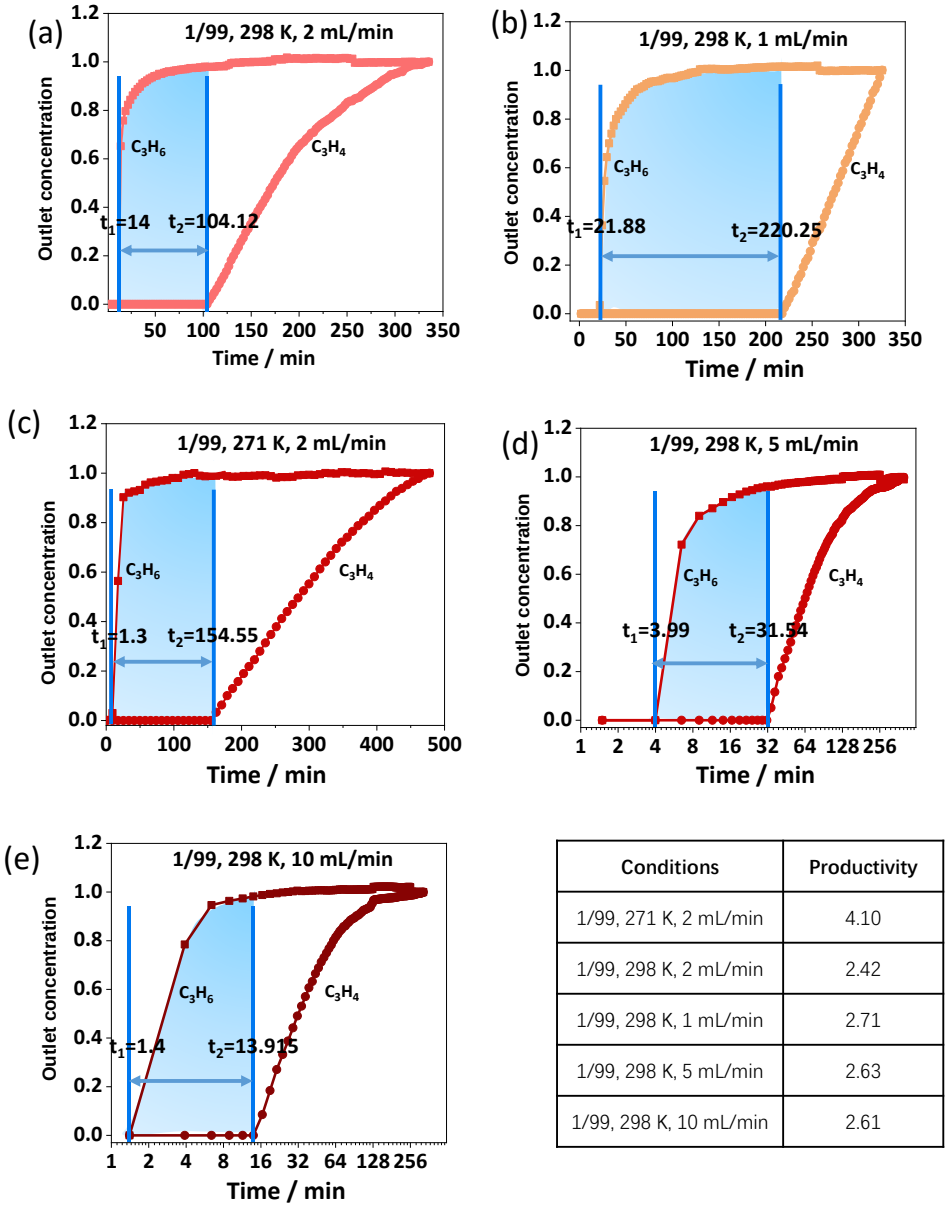

Conditions	Productivity
1/99, 271 K, 2 mL/min	4.10
1/99, 298 K, 2 mL/min	2.42
1/99, 298 K, 1 mL/min	2.71
1/99, 298 K, 5 mL/min	2.63
1/99, 298 K, 10 mL/min	2.61

Figure S42. The calculation of C_3H_6 productivity during the 1/99 C_3H_4/C_3H_6 breakthrough process in **NTU-88** (a: 1/99, 298 K, 2 mL/min; b: 1/99, 298 K, 1 mL/min; c: 1/99, 271 K, 2 mL/min; d: 1/99, 298 K, 5 mL/min; e: 1/99, 298 K, 10 mL/min). The sample weight is 3.05 g. The C_3H_6 productivity is defined by the breakthrough amount of C_3H_6, which is calculated by integration of the breakthrough curves *f(t)* during a period from *t1* to *t2* where the C_3H_6 purity is higher than or equal to the value of 99.95%:

$$q_{C_3H_6} = \left(\frac{C_i(C_3H_6)}{C_i(C_3H_6)+C_i(C_3H_4)}\right) \times \int_{t1}^{t2} f(dt) \times FC_3H_6, out)/m_{pcp}.$$

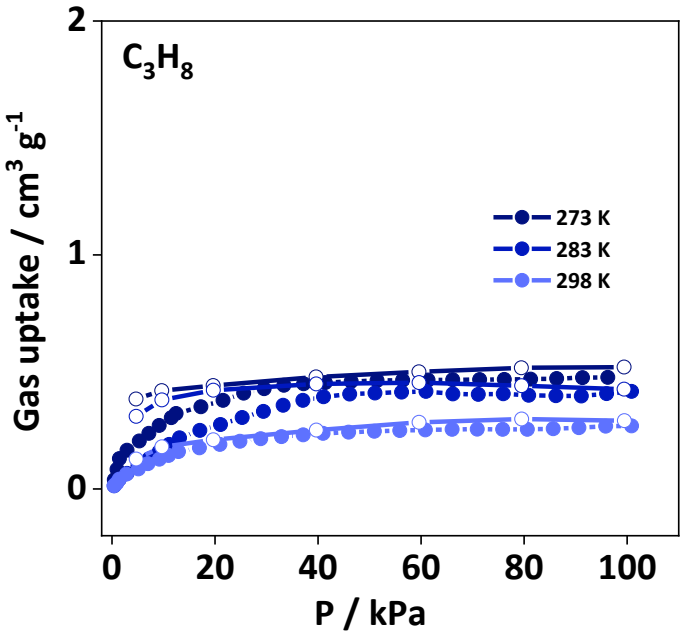

Figure S43. C_3H_8 adsorption isotherms of **NTU-88a** at different temperatures.

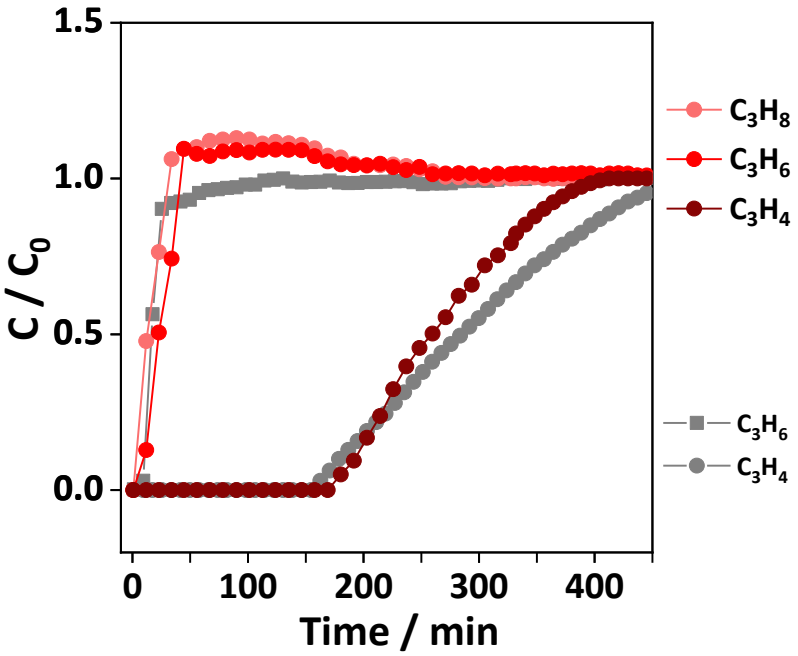

Figure S44. Comparsion of breakthrough curves of **NTU-88a** with ternary (C_3H_4/C_3H_6/C_3H_8: 0.95/94.05/5, v/v/v, 2 mL/min) and binary (C_3H_4/C_3H_6: 1/99, v/v, 2 mL/min) feed gas at 273K. Along with the above single-component isotherms (S43) and this ternary breakthrough result, it is rational to know that C_3H_8 has negligible effect on the ability of exclusive C_3H_4 capture.

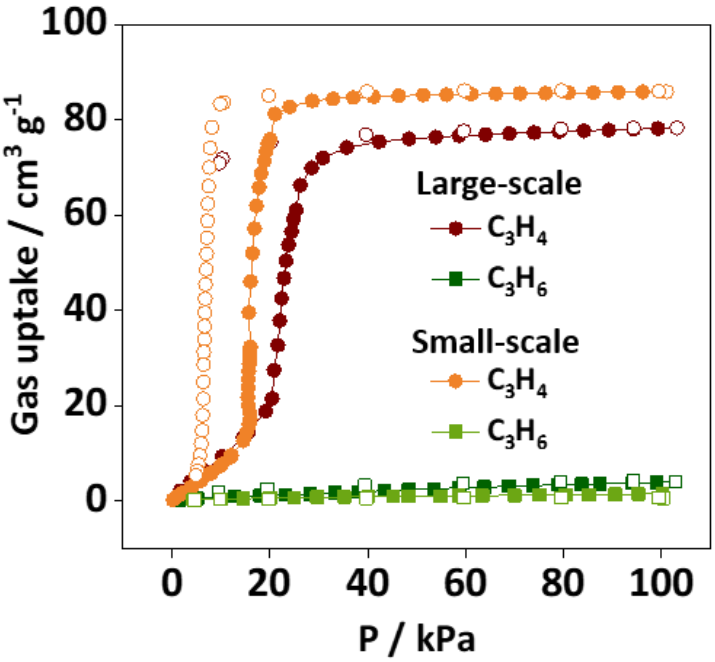

Figure S45. C_3H_4 and C_3H_6 adsorption isotherms of the large-scale and small-scale synthesized **NTU-88** at 298K.

Table S1. Crystal data of **NTU-88**

Name	NTU-88
Formula	$C_{20}H_{18}Cl_2N_6Ni$
Formula weight	471.99
Crystal System	orthorhombic
Space group	*P*bcn
a / Å	13.065(5)
b / Å	18.273(7)
c / Å	14.809(6)
V / Å^3	3536(2)
Z	4
*D*calc /gcm^{-3}	1.003
Mu(MoKa) /mm^{-1}	0.71073
F(000)	1056
Θ range^o	1.9, 27.3
Index ranges	-15 ≤ h ≤ 14 -22 ≤ k ≤ 22 -19 ≤ l ≤ 18
Tot., Uniq. Data	25949,3766
R(int)	0.062
Observed Data [I > 2.0 sigma(I)]	2780
R_1	0.0426
wR_2	0.1138
GOOF	1.05

$R_1 = \Sigma||Fo| - |Fc||/|Fo|$; $wR_2 = [\Sigma w(\Sigma Fo^2 - Fc^2)^2/\Sigma w(Fo^2)^2]^{1/2}$

Table S2. Hydrogen bonds of the frameworks.

	D--H···A	Bonding distance of H···A (Å)	Angle (°)
NTU-88	C8--H8···Cl1	3.003	109.335
	C4--H4···Cl1	2.824	117.542
	C5--H5···Cl1	2.798	111.668
	C11--H11···Cl1	2.707	121.074
	N3--H3···Cl1	2.363	159.077
NTU-88c	C1--H1···Cl1	2.730	97.852
	C5--H5···Cl1	3.106	93.453
	C6--H6···Cl1	2.403	111.815
	C10--H10···Cl1	2.404	108.536
	N3--H3···Cl1	2.878	140.710
NTU-88α	C1--H1···Cl1	2.720	98.102
	C5--H5···Cl1	3.057	95.206
	C6--H6···Cl1	2.409	111.309
	C10--H10···Cl1	2.406	108.579
	N3--H3···Cl1	2.970	136.873
NTU-88β	C1--H1···Cl1	2.714	98.228
	C5--H5···Cl1	3.043	95.562
	C6--H6···Cl1	2.407	111.385
	C10--H10···Cl1	2.404	108.603
	N3--H3···Cl1	3.015	135.551
NTU-88o⊃ C_3H_4	C24--H7···C17	2.740	116.994
	C24--H7···C15	2.784	101.486
	C26--H30···C20	2.921	115.634
	C26--H29···C8	2.904	98.934
	C26--H28···C6	2.817	135.313
	C26--H28···C8	2.731	109.359

Table S3. Crystal data and structure refinement of **NTU-88** at different states.

Name	**NTU-88c**	**NTU-88α**	**NTU-88β**	**NTU-88o⊃C_3H_4**
Formula	$C_{20}H_{18}Cl_2N_6Ni$	$C_{20}H_{18}Cl_2N_6Ni$	$C_{20}H_{18}Cl_2N_6Ni$	$C_{20}H_{18}Cl_2N_6Ni$, 2(C_3H_4)
Formula weight	471.99	471.99	471.99	552.12
Crystal System	monoclinic	monoclinic	monoclinic	monoclinic
Space group	$P2_1/c$	$P2_1/c$	$P2_1/c$	$P2_1/c$
a / Å	9.009(2)	9.073(4)	9.114(5)	8.6953
b / Å	16.202(3)	16.193(6)	16.184(6)	15.2824
c / Å	8.742(1)	8.984(3)	9.020(3)	10.1447
V / Å^3	1121.4(4)	1158.2(8)	1165.1(9)	1182.54
β	118.496	118.66	118.87	118.6931
Z	2	2	2	2
*D*calc /gcm^{-3}	1.398	1.353	1.345	1.551

Table S4. Comparison of gas uptakes, C_3H_4/C_3H_6 uptake ratios, purity of desorbed C_3H_4 and productivity of C_3H_6 for various porous materials at 298K.

Adsorbents	C_3H_4 uptake (cm^3/g)			C_3H_6 uptake (cm^3/g)			C_3H_4/C_3H_6 uptake ratio			Purity of desorbed C_3H_4	Productivity of C_3H_6 (mmol/g)	Refs
	1 bar	0.2 bar	0.01 bar	1 bar	0.8 bar	0.99 bar	1/1	0.2/0.8	0.01/0.99			
NTU-88	85.90	75.96	1.02	1.63	1.33	1.62	52.70	57.11	0.62	99.95%	4.10 at 271 K 2.42 at 298 K	This work
GeFSIX-dps-Cu	82.88	74.37	9.18	1.79	1.78	1.79	46.25	41.78	5.13	99.99%	-	[6]
ZJUT-1	51.07	30.05	8.96	18.83	17.02	18.82	2.71	1.77	0.47	-	17.86	[7]
UTSA-200	80.2	76.09	66.98	26.88	26.65	26.88	2.98	2.86	2.49	-	62.05	[8]
NbOFFIVE-1-Ni	42.30	38.98	38.08	27.50	25.98	27.50	1.54	1.50	1.38	-	-	[9]
ZU-13	86.91	71.46	48.83	31.36	30.68	31.18	2.77	2.33	1.57	-	57.14	[10]
ELM-12	62.0	59.20	40.77	32.04	30.09	32.03	1.83	1.97	1.27	-	15.36	[11]
SIFSIX-3-Zn	50.62	47.30	45.92	42.17	39.87	40.32	1.20	1.19	1.14	-	-	[9]
NKMOF-1-Ni	78.4	57.86	41.44	46.0	42.01	45.92	1.70	1.38	0.90	-	-	[12]
sql-NbOFFIVE-bpe-Cu-AB	65.07	57.12	42.90	47.04	45.83	46.88	1.38	1.25	0.92	-	118.0	[13]
SIFSIX-2-Cu-i	92.5	70.22	43.90	59.6	56.22	58.91	1.30	1.25	0.74	-	26.34	[9]
ZU-62	83.0	75.71	49.06	60.58	57.60	59.81	1.37	1.31	0.82	-	-	[14]
SIFSIX-3-Ni	64.59	62.83	57.34	61.51	58.46	60.93	1.05	1.07	0.98	-	19.02	[9]
UiO-66	229.15	162.2	35.39	74.59	70.02	74.59	3.07	2.32	0.47	-	0.9	[8]
ZIF-8	140.45	71.70	2.91	91.17	87.00	91.17	1.54	0.82	0.03	-	1.3	[8]
SIFSIX-Cu-TPA	188.31	162.4	103.73	130.05	127.4	129.92	1.45	1.27	0.80	-	52.9	[15]
SIFSIX-1-Cu	196.2	169.7	57.57	132.2	128.58	131.71	1.25	1.56	0.44	-	4.46	[9]
MIL-100(Cr)	325.02	165.4	34.05	140.0	131.8	140.0	2.32	1.25	0.24	-	-	[8]
Fe-MOF-74	177.86	160.0	48.83	148.51	146.2	148.51	1.20	1.09	0.33	-	-	[16]
Cu-BTC	378.78	293.8	32.93	209.44	206.0	209.4	1.81	1.43	0.16	-	2.77	[8]

Table S5. Dual-site Langmuir-Freundlich fits for C_3H_4, and C_3H_6 in **NTU-88**.

	Site A				Site B			
	$\frac{q_{A.sat}}{\text{mol kg}^{-1}}$	$\frac{b_{A,0}}{\text{Pa}^{-\nu_A}}$	$\frac{E_A}{\text{kJ mol}^{-1}}$	ν_A	$\frac{q_{B.sat}}{\text{mol kg}^{-1}}$	$\frac{b_{B,0}}{\text{Pa}^{-\nu_B}}$	$\frac{E_B}{\text{kJ mol}^{-1}}$	ν_B
C_3H_4	0.5	7.175E-10	29.4	1	3.35	7.404E-172	634	14.2
C_3H_6	0.075	6.794E-10	27	1				

Notation for calculation of adsorption heats

b Langmuir-Freundlich constant, $\text{Pa}^{-\nu}$

E energy parameter, J mol^{-1}

q component molar loading of species *i*, mol kg^{-1}

q_{sat} saturation loading, mol kg^{-1}

Q_{st} isosteric heat of adsorption, J mol^{-1}

T absolute temperature, K

References

[1] R. S. Alekseev, A. V. Kurkin, M. A. Yurovskaya, *Chem. Heterocycl. Compd. (N. Y., NY, U. S.)* **2012**, *48*, 1235.
[2] G. M. Sheldrick, *Acta Crystallogr. Sec. A* **2008**, *64*, 112.
[3] L. Y. Wang, N. Xu, Y. Q. Hu, W. Q. Sun, R. Krishna, J. H. Li, Y. J. Jiang, S. Duttwyler, Y. B. Zhang, *Nano Res* **2023**, *16*, 3536.
[4] M. J. e. a. Frisch, Gaussian, Inc., Wallingford CT, **2016**.
[5] K. Momma, F. Izumi, *J. Appl. Crystallogr.* **2011**, *44*, 1272.
[6] T. Ke, Q. J. Wang, J. Shen, J. Y. Zhou, Z. B. Bao, Q. W. Yang, Q. L. Ren, *Angew. Chem. Int. Ed.* **2020**, *59*, 12725.
[7] H. M. Wen, L. B. Li, R. B. Lin, B. Li, B. Hu, W. Zhou, J. Hu, B. L. Chen, *J. Mater. Chem. A* **2018**, *6*, 6931.
[8] L. B. Li, H. M. Wen, C. H. He, R. B. Lin, R. Krishna, H. Wu, W. Zhou, J. P. Li, B. Li, B. L. Chen, *Angew. Chem. Int. Ed.* **2018**, *57*, 15183.
[9] L. F. Yang, X. L. Cui, Q. W. Yang, S. H. Qian, H. Wu, Z. B. Bao, Z. G. Zhang, Q. L. Ren, W. Zhou, B. L. Chen, H. B. Xing, *Adv. Mater.* **2018**, *30*, 1705374.
[10] L. F. Yang, X. L. Cui, Y. B. Zhang, Q. W. Yang, H. B. Xing, *J. Mater. Chem. A* **2018**, *6*, 24452.
[11] L. B. Li, R. B. Lin, R. Krishna, X. Q. Wang, B. Li, H. Wu, J. P. Li, W. Zhou, B. L. Chen, *J. Am. Chem. Soc.* **2017**, *139*, 7733.
[12] Y. L. Peng, C. He, T. Pham, T. Wang, P. Li, R. Krishna, K. A. Forrest, A. Hogan, S. Suepaul, B. Space, M. Fang, Y. Chen, M. J. Zaworotko, J. Li, L. Li, Z. Zhang, P. Cheng, B. Chen, *Angew. Chem. Int. Ed.* **2019**, *58*, 10209.
[13] M. Y. Gao, A. A. Bezrukov, B. Q. Song, M. He, S. J. Nikkhah, S. Q. Wang, N. Kumar, S. Darwish, D. Sensharma, C. Deng, J. Li, L. Liu, R. Krishna, M. Vandichel, S. Yang, M. J. Zaworotko, *J .Am. Chem. Soc.* **2023**, *145*, 11837.
[14] L. F. Yang, X. L. Cui, Z. Q. Zhang, Q. W. Yang, Z. B. Bao, Q. L. Ren, H. B. Xing, *Angew. Chem. Int. Ed.* **2018**, *57*, 13145.
[15] Y. Jiang, L. Wang, T. Yan, J. Hu, W. Sun, R. Krishna, D. Wang, Z. Gu, D. Liu, X. Cui, H. Xing, Y. Zhang, *Chem. Sci.* **2023**, *14*, 298.
[16] E. D. Bloch, W. L. Queen, R. Krishna, J. M. Zadrozny, C. M. Brown, J. R. Long, *Science* **2012**, *335*, 1606.